

# Resolving the nano-Hz gravitational wave sky: the detectability of eccentric binaries with PTA experiments

Riccardo J. Truant<sup>1,\*</sup>, David Izquierdo-Villalba<sup>1,2</sup>, Alberto Sesana<sup>1,2</sup>,  
Golam Mohiuddin Shaifullah<sup>1,2</sup>, and Matteo Bonetti<sup>1,2,3</sup>

<sup>1</sup> Dipartimento di Fisica “G. Occhialini”, Università degli Studi di Milano-Bicocca, Piazza della Scienza 3, I-20126 Milano, Italy

<sup>2</sup> INFN, Sezione di Milano-Bicocca, Piazza della Scienza 3, 20126 Milano, Italy

<sup>3</sup> INAF - Osservatorio Astronomico di Brera, via Brera 20, I-20121 Milano, Italy

Received —; accepted —

## ABSTRACT

Pulsar Timing Array (PTA) collaborations reported evidence of a nano-Hz stochastic gravitational wave background (sGWB) compatible with an adiabatically inspiraling population of massive black hole binaries (MBHBs). Despite the large uncertainties, the relatively flat spectral slope of the recovered signal suggests a possible prominent role of MBHB dynamical coupling with the environment or/and the presence of an eccentric MBHB population. This work aims at studying the capabilities of future PTA experiments to detect single MBHBs under the realistic assumption that the sGWB is originated from an eccentric binary population coupled with its environment. To this end, we generalize the standard signal-to-noise ratio (SNR) and Fisher Information Matrix calculations used in PTA for circular MBHBs to the case of eccentric systems. We consider an ideal 10-year MeerKAT and 30-year SKA PTAs and apply our method over a wide number of simulated eccentric MBHB populations. We find that the number of resolvable MBHBs for the SKA (MeerKAT) PTA is  $\sim 30$  (4) at  $\text{SNR} > 5$  ( $> 3$ ), featuring an increasing trend for larger eccentricity values of the MBHB population. This is the result of eccentric MBHBs at  $\lesssim 10^{-9}$  Hz emitting part of their power at high harmonics, thus reaching the PTA sensitivity band. Our results also indicate that resolved MBHBs do not follow the eccentricity distribution of the underlying MBHB population, but prefer low eccentricity values ( $< 0.6$ ). Finally, the recovery of binary intrinsic properties and sky-localization do not depend on the system eccentricity, while orbital parameters such as eccentricity and initial orbital phase show clear trends. Although simplified, our results show that SKA will enable the detection of tens of MBHBs, projecting us into the era of precision gravitational wave astronomy at nano-Hz frequencies.

**Key words.** black hole physics – gravitational waves – methods: numerical – methods: statistical

## 1. Introduction

In the last three decades, multi-wavelength observations have pointed out that massive black holes ( $> 10^6 M_{\odot}$ , MBHs) reside at the centre of most of the galaxies, co-evolving with them and powering quasars and active galactic nuclei (Schmidt 1963; Genzel & Townes 1987; Kormendy 1988; Dressler & Richstone 1988; Kormendy & Richstone 1992; Haehnelt & Rees 1993; Genzel et al. 1994; Faber 1999; O’Dowd et al. 2002; Häring & Rix 2004; Peterson et al. 2004; Vestergaard & Peterson 2006; Hopkins et al. 2007; Merloni & Heinz 2008; Kormendy & Ho 2013; Ueda et al. 2014; Savorgnan et al. 2016). Galaxies do not evolve in isolation and, in the context of the currently favored hierarchical clustering scenario for structure formation, they are expected to merge frequently (White & Rees 1978; White & Frenk 1991; Lacey & Cole 1993). Consequently, the presence of MBHs lurking in the centers of galaxies and the important role of galactic mergers suggest that massive black hole binaries (MBHBs) have formed and coalesced throughout cosmic history.

The dynamical evolution of MBHBs is ruled by many different processes (see e.g. the seminal work by Begelman et al. 1980). Following the merger of the two parent galaxies, dynamical friction, exerted by dark matter stars and gas, drags the two MBHs towards the nucleus of the newly formed system,

reducing the initial MBH separation ( $\sim$  kpc scales) down to a few parsecs (Yu 2002; Mayer et al. 2007; Fiacconi et al. 2013; Bortolas et al. 2020, 2022; Li et al. 2022). At these distances, a bound binary forms and dynamical friction ceases to be efficient. Interactions with single stars or torques extracted from a circumbinary gaseous disc take the main role in further evolving the MBHB separation (Quinlan & Hernquist 1997; Sesana et al. 2006; Vasiliev et al. 2014; Sesana & Khan 2015; Escala et al. 2004; Dotti et al. 2007; Cuadra et al. 2009; Bonetti et al. 2020; Franchini et al. 2021, 2022). These processes harden the MBHB down to sub-pc scales, where the emission of gravitational waves (GWs) drives it to final coalescence. During this last evolutionary stage, MBHBs are powerful GW sources, whose emission spans over a wide range of frequencies. In particular, low- $z$ , high mass ( $> 10^7 M_{\odot}$ ) inspiralling MBHBs emit GWs in the nano-Hz frequency window ( $10^{-9} - 10^{-7}$  Hz), probed by Pulsar Timing Array (PTA) experiments (Foster & Backer 1990).

By monitoring an array of millisecond pulsars and measuring the changes in the time-of-arrival of their pulses, PTAs are sensitive to the incoherent superposition of all the GWs coming from the cosmic population of MBHBs (Sazhin 1978; Deweiler 1979). The overall signal is thus expected to have the properties of a stochastic GW background (sGWB). The specific amplitude and spectral shape of the signal are closely related to the galaxy merger rate and the environment in which MBHBs shrink (Phinney 2001; Jaffe & Backer 2003; Kocsis & Sesana

\* r.truant@campus.unimib.it

2011; Sesana 2013a; Ravi et al. 2014), and it can be disentangled from other stochastic noise processes affecting PTA measurements thanks to its distinctive correlation properties (Hellings & Downs 1983). Moreover, because of the sparseness of the most massive and nearby binaries, individual deterministic signals, usually referred to as continuous GWs (CGWs) might also be resolved (Sesana et al. 2009; Rosado et al. 2015; Agazie et al. 2023a; Antoniadis et al. 2023). Those would provide precious information about the most massive and nearby MBHBs in the universe and are ideal targets to extend multimessenger astronomy in the nano-Hz GW band (e.g. Burke-Spolaor 2013). For this reason, both types of signals (CGW and sGWB) are of great interest for PTA observations.

There is currently several operational PTA collaborations around the world: the *European Pulsar Timing Array* (EPTA, Kramer & Champion 2013; Desvignes et al. 2016), the *North American Nanohertz Observatory for Gravitational Waves* (NANOGrav, McLaughlin 2013; Arzoumanian et al. 2015), the *Parkes Pulsar Timing Array* (PPTA, Manchester et al. 2013; Reardon et al. 2016), the *Indian PTA* (InPTA, Susobhanan et al. 2021), the *Chinese PTA* (CPTA, Lee 2016) and the *MeerKAT PTA* (MPTA, Miles et al. 2023). The latest results published by several of those collaborations report evidence about the presence of an sGWB (at  $2 - 4\sigma$  significance level, EPTA Collaboration et al. 2023a; Agazie et al. 2023b; Reardon et al. 2023; Xu et al. 2023), compatible with the existence of low- $z$  MBHBs (Afzal et al. 2023; EPTA Collaboration et al. 2024). Quite interestingly, the amplitude of the signal is at the upper end of the predicted range of MBHB populations (see e.g. Sesana 2013b), and the best fit to the logarithmic spectral slope of the signal appears to deviate from the vanilla  $-2/3$  value, expected from a circular population of MBHBs evolving solely through GW emission. Although uncertainties are too large to draw any conclusion, these two facts might bear important implications for the underlying MBHB population. On the one hand, the high signal amplitude likely implies a large contribution from very massive binaries at the upper-end of the MBH mass function. On the other hand, the tentative deviation in the spectral slope can hint at a strong coupling of the binaries with their stellar environment (i.e. stellar hardening, Quinlan & Hernquist 1997; Sesana et al. 2006) or at non-negligible orbital eccentricities (see e.g. Gualandris et al. 2022; Fastidio et al. 2024).

In light of the above considerations, it is therefore interesting to investigate the expected statistical properties of CGWs that might be resolved by future PTA experiments. In fact, although the topic has been addressed by several authors (e.g. Rosado et al. 2015; Kelley et al. 2018; Gardiner et al. 2023), most of the current literature focuses on fairly idealised cases. Both Rosado et al. (2015) and Gardiner et al. (2023) assume circular binaries, and a vast range of models that are not necessarily tailored to the currently detected signal. Kelley et al. (2018) brings eccentricity in the picture, but employs a very simplified description of the signal and investigates a scenario where the GWB is almost a factor of three smaller than what currently inferred from the data. Moreover, none of the work above touches on PTA capabilities to estimate the source parameters. Work on this subject has so far involved only circular binaries (e.g. Sesana & Vecchio 2010; Ellis et al. 2012; Goldstein et al. 2019) and when eccentricity has been considered (Taylor et al. 2016), results have never been scaled at the overall MBHB population level.

In this work, we aim to relax several of the assumptions made in previous investigations with the goal of providing an extensive assessment of future PTA experiments capabilities of resolving CGWs. To this end, we employ state-of-the-art MBHB popula-

tions including environmental coupling and eccentricity, tailored to reproduce the observed PTA signal. We also adapt the formalism of Barack & Cutler (2004) to PTA sources to develop a fast Fisher Information Matrix algorithm for eccentric binaries, limiting the description of the signal to the Earth term only. We apply this machinery to putative 10-year MeerKAT and 30-year SKA PTAs, and we identify resolvable CGWs via iterative subtraction (Karnesis et al. 2021) over a wide range of simulated eccentric MBHB populations compatible with the latest amplitude of the sGWB, offering a realistic assessment of the future potential of PTAs.

The paper is organized as follows. In Section 2 we overview the methodology used to characterize the emission of eccentric MBHBs and the time residuals that they imprint in PTA data. In Section 3, we describe the computation of the signal-to-noise ratio and Fisher Information Matrix for eccentric MBHBs. In Section 4, we present the population of eccentric MBHBs and the PTA experiments that we use. In Section 5, we discuss the results, focusing on the number of resolvable sources and the effect of the eccentricity in determining their number and their parameter estimation. In Section 6, we discuss some of the caveats of the present implementation and finally, in Section 7, we summarise the main results of the paper. A Lambda Cold Dark Matter ( $\Lambda$ CDM) cosmology with parameters  $\Omega_m = 0.315$ ,  $\Omega_\Lambda = 0.685$ ,  $\Omega_b = 0.045$ ,  $\sigma_8 = 0.9$  and  $h = H_0/100 = 67.3/100 \text{ km s}^{-1} \text{ Mpc}^{-1}$  is adopted throughout the paper (Planck Collaboration et al. 2014).

## 2. The gravitational emission of eccentric supermassive black holes binaries

In this section, we outline the basic concepts used to explore the detectability of CGWs generated by eccentric MBHBs.

### 2.1. The gravitational wave signal

The GW metric perturbation  $h_{ab}(t)$  in the trace-less and transverse (TT) gauge can be written as a linear superposition of two polarizations ( $h_+$  and  $h_\times$ ) and their base tensor ( $e_{ab}^+$  and  $e_{ab}^\times$ ):

$$h_{ab}(t, \hat{\Omega}) = h_+(t)e_{ab}^+(\hat{\Omega}) + h_\times(t)e_{ab}^\times(\hat{\Omega}) \quad (1)$$

where  $\hat{\Omega}$  is the GW propagation direction. Differently from the monochromatic emission of a circular binary, the GW signal of an eccentric source is spread over a spectrum of harmonics of the orbital frequency. To model the signal of these eccentric sources, we use the GW waveform presented in Taylor et al. (2016), which provides the analytic expression of the GW emission of an eccentric binary. Specifically, adopting the quadrupolar approximation and making use of the Fourier analysis of the Kepler problem,  $h_{+, \times}$  can be written as:

$$\begin{aligned} h_+(t) &= \sum_{n=1}^{\infty} -\left(1 + \cos^2 \iota\right) \left[ a_n \cos(2\gamma) - b_n \sin(2\gamma) \right] + \left(1 - \cos^2 \iota\right) c_n, \\ h_\times(t) &= \sum_{n=1}^{\infty} 2 \cos \iota \left[ b_n \cos(2\gamma) + a_n \sin(2\gamma) \right], \end{aligned} \quad (2)$$

where

$$\begin{aligned} a_n &= -n\zeta\omega^{2/3}J_{n-2}(ne) - 2eJ_{n-1}(ne) + (2/n)J_n(ne) \\ &\quad + 2eJ_{n+1}(ne) - J_{n+2}(ne)\cos(nl(t)), \\ b_n &= -n\zeta\omega^{2/3}\sqrt{1-e^2}[J_{n-2}(ne) - 2J_n(ne) + J_{n+2}(ne)]\sin(nl(t)), \\ c_n &= 2\zeta\omega^{2/3}J_n(ne)\cos(nl(t)). \end{aligned} \quad (3)$$

being  $e$  the eccentricity of the MBHB,  $n$  the harmonic number and  $J_n(x)$  the  $n$ -th Bessel Function of the first kind.  $\zeta$  is the GW amplitude given by the combination of the redshifted chirp mass,  $\mathcal{M}_z$ , and the luminosity distance,  $D_L$ :

$$\zeta = \frac{(G\mathcal{M}_z)^{5/3}}{c^4 D_L}. \quad (4)$$

Here,  $c$  is the light speed and  $G$  is the gravitational constant. The redshifted chirp mass is expressed as:

$$\mathcal{M}_z = \mathcal{M}(1+z) = \frac{Mq^{5/3}}{(1+q)^{6/5}}(1+z), \quad (5)$$

being  $\mathcal{M}$  the rest-frame chirp mass,  $M = m_1 + m_2$  the total mass of the binary in the rest frame, and  $q = m_2/m_1 < 1$  its mass ratio. With this definition of  $q$ ,  $m_1$  and  $m_2$  are identified as the mass of the primary and secondary MBH, respectively. The variable  $\iota$  is the inclination angle defined as the angle between the GW propagation direction and the binary orbital angular momentum,  $\hat{L}$ . The quantity  $l(t)$  refers to the binary mean anomaly  $l(t) = l_0 + 2\pi \int_{t_0}^t f_k(t') dt'$ , where  $f_k(t')$  corresponds to the observed Keplerian frequency defined as  $f_k(t) = (1+z)f_{k,r}(t)$  with  $f_{k,r}(t) = (2\pi)^{-1} \sqrt{GM/r_{bin}(t)^3}$  the rest frame Keplerian frequency and  $r_{bin}(t)$  the semi-major axis of the MBHB orbit. In principle,  $r_{bin}(t)$  can evolve during the observation time due to the GW emission and environmental interaction. However, here we assume that the orbital frequency and eccentricity do not evolve during the observation time and, hence,  $f_k(t)$  can be treated as a constant value, i.e.  $f_k$  (see discussion about this assumption in Section 6). The orbital angular frequency is then given by  $\omega = 2\pi f_k$ , while  $\gamma$  is the angle that measures the direction of the pericenter with respect to the direction  $\hat{x}$ , defined as  $\hat{x} \equiv (\hat{\Omega} + \hat{L} \cos i) / \sqrt{1 - \cos^2 i}$ .

## 2.2. The timing residuals

A GW passing between the pulsar and the Earth perturbs the space-time metric, causing a modification in the arrival time of the pulse to the Earth. This induces a fractional shift in the pulsar rotational frequency,  $z(t, \hat{\Omega})$ , given by (e.g. Anholm et al. 2009; Book & Flanagan 2011):

$$z(t, \hat{\Omega}) = \frac{1}{2} \frac{p^a p^b}{1 + \hat{\Omega} \cdot \hat{p}} \Delta h_{ab}, \quad (6)$$

where  $\hat{p}$  is the unit direction vector to the pulsar and  $\Delta h_{ab} = h_{ab}(t, \mathbf{x}_E) - h_{ab}(t_P, \mathbf{x}_P)$  is the difference in the metric perturbation computed at the moment in which the GW arrives at the solar system barycenter ( $t$ ), and when it passed through the pulsar ( $t_P = t - L/c$ , where  $L$  denotes the distance to the pulsar). We define  $\mathbf{x}_E$  to coincide with the solar system barycenter, which is the origin of the adopted coordinate system, while  $\mathbf{x}_P = L\hat{p}$

corresponds to the pulsar sky position. In practice, what PTA experiments measure is the *timing residual*, which corresponds to the time integrated effect of Eq. (6):

$$\begin{aligned} s(t) &= \int_{t_0}^t dt' z(t') \\ &= F^+(\hat{\Omega}) [s_+(t) - s_+(t_0)] + F^\times(\hat{\Omega}) [s_\times(t) - s_\times(t_0)]. \end{aligned} \quad (7)$$

Here,  $s_{+, \times}(t) = \int_{t_0}^t h_{+, \times}(t') dt'$ ,  $t_0$  is the time at which the observational campaign starts and  $t = t_0 + T_{\text{obs}}$  is the epoch of the considered observation. The variable  $F^{+, \times}$  denote the *antenna pattern functions* and encode the geometrical properties of the detector (for a PTA experiment the test masses are the Earth and the pulsar). In particular,  $F^{+, \times}$  depends on the GW propagation direction ( $\hat{\Omega}$ ) and the pulsar sky location ( $\hat{p}$ ). By making use of the polarization basis tensor  $\{\hat{n}, \hat{u}, \hat{v}\}$  (see Taylor 2021), the pattern functions  $F^{+, \times}$  can be written as:

$$F^+(\hat{\Omega}) = \frac{1}{2} \frac{[\hat{u} \cdot \hat{p}]^2 - [\hat{v} \cdot \hat{p}]^2}{1 + \hat{\Omega} \cdot \hat{p}}, \quad (8)$$

and

$$F^\times(\hat{\Omega}) = \frac{[\hat{u} \cdot \hat{p}][\hat{v} \cdot \hat{p}]}{1 + \hat{\Omega} \cdot \hat{p}}, \quad (9)$$

where  $\hat{n}$  corresponds to the vector pointing to the GW source:

$$\hat{n} = -\hat{\Omega} = [\cos \theta \cos \phi, \cos \theta \sin \phi, \sin \theta], \quad (10)$$

and  $\hat{u}$  and  $\hat{v}$  are defined as:

$$\begin{aligned} \hat{u} = \frac{\hat{n} \times \hat{L}}{|\hat{n} \times \hat{L}|} &= [\cos \psi \sin \theta \cos \phi - \sin \psi \cos \theta, \\ &\quad \cos \psi \sin \theta \sin \phi + \sin \psi \cos \theta, \\ &\quad -\cos \psi \cos \theta], \end{aligned} \quad (11)$$

$$\begin{aligned} \hat{v} = \hat{u} \times \hat{n} &= [\sin \psi \sin \theta \cos \phi + \cos \psi \sin \phi, \\ &\quad \sin \psi \sin \theta \sin \phi - \cos \psi \cos \phi, \\ &\quad -\sin \psi \cos \theta]. \end{aligned} \quad (12)$$

Here  $\theta$  and  $\phi$  are the sky location of the MBHB expressed in spherical polar coordinates  $(\theta, \phi) = (\pi/2 - \text{DEC}, \text{RA})$ , being DEC the declination and RA the right ascension of the binary. Finally,  $\psi$  is the polarization angle, ranging between  $[0, \pi]$ .

For simplicity, we consider only the Earth term<sup>1</sup>, we ignore any time evolution of the MBHB frequency and neglect higher-order post-Newtonian effects such as the pericenter precession and orbit-spin coupling. Those are expected to play a minor role in the output of PTA GW signal (Sesana & Vecchio 2010), and can be safely neglected, at least for a first order estimate. We will comment on the validity of these assumptions in Section 6. Under the framework outlined above, the values of the timing residuals can be written analytically as (Taylor et al. 2016):

$$\begin{aligned} s_+(t) &= \sum_{n=1}^{\infty} -\left(1 + \cos^2 i\right) \left[\tilde{a}_n \cos(2\gamma) - \tilde{b}_n \sin(2\gamma)\right] \\ &\quad + \left(1 - \cos^2 i\right) \tilde{c}_n, \\ s_\times(t) &= \sum_{n=1}^{\infty} 2 \cos i \left[\tilde{b}_n \cos(2\gamma) + \tilde{a}_n \sin(2\gamma)\right], \end{aligned} \quad (13)$$

<sup>1</sup> For further information about the impact of including the pulsar distance in the computation of the SNR, we refer to Taylor et al. 2016.

being:

$$\begin{aligned}\tilde{a}_n &= -\zeta\omega^{-1/3}[J_{n-2}(ne) - 2eJ_{n-1}(ne)(2/n)J_n(ne) \\ &\quad + 2eJ_{n+1}(ne) - J_{n+2}(ne)]\sin(nl(t)) \\ \tilde{b}_n &= \zeta\omega^{-1/3}\sqrt{1-e^2}[J_{n-2}(ne) - 2J_n(ne) + J_{n+2}(ne)]\cos(nl(t)) \\ \tilde{c}_n &= (2/n)\zeta\omega^{-1/3}J_n(ne)\sin(nl(t)).\end{aligned}\quad (14)$$

### 3. SNR and parameter estimation of supermassive black hole binaries in PTA data

In this section, we introduce the methodology used to compute the *signal-to-noise ratio* (hereafter, SNR) and the *Fisher information matrix* from the gravitational wave signal emitted by a single eccentric MBHB.

#### 3.1. Signal-to-noise ratio for eccentric binaries

In general, to assess the possibility of detecting a nano-Hz CGW signal generated by an MBHB it is required to determine how its signal compares with the background noise present in the detector. This is usually done by computing the SNR. Given the deterministic nature of the CGW signal, the optimal way to compute the SNR is through *matched filtering*. Assuming that a CGW is present in the timing residual of a pulsar, the match filtering procedure gives the expression:

$$\left(\frac{S}{N}\right)^2 = 4 \int_0^\infty df \frac{|\tilde{s}(f)|^2}{S_k(f)}. \quad (15)$$

Estimating the SNR therefore requires the characterization of the noise properties encoded in  $S_k(f)$ , i.e the noise power spectral density (NPSD) of the  $k$ -th pulsar inside our array, besides the knowledge of the signal  $\tilde{s}(f)$ , which is the Fourier transforms of  $s(t)$  given by Eq. (13).

As shown by Eq. (15), the computation of the SNR requires the time residuals in the frequency domain, i.e.  $\tilde{s}(f)$ . However, as described in Section 2.1, in PTA experiments the time residuals are framed on the time domain. Transforming these in the frequency domain can be easily addressed in the case of circular binaries given that the CGW signal is monochromatic (see e.g. Rosado et al. 2015). However, in the generic case of an eccentric binary, the signal is spread over a spectrum of harmonics and the term  $|\tilde{s}(f)|^2$  contains mixed products between residuals originated at different harmonics. To address this scenario we worked under the assumption that the noise is a Gaussian and zero-mean stochastic stationary process and adopted a similar approach to the one presented in Barack & Cutler (2004). In brief, even if Eq. (15) is given by the mixed product generated by different harmonics, their signal in the frequency domain is described by a delta function centred at the emission frequency  $nf_k$ . Consequently, the product of the residuals generated by harmonics emitting at different frequencies are orthogonal and cancel out. We can therefore treat each harmonic separately as a monochromatic signal and compute its SNR by exploiting the fact that

$$\frac{4}{S_k(f_n)} \int_0^\infty |\tilde{s}_n(f)|^2 df \simeq \frac{2}{S_k(f_n)} \int_0^\infty s_n(t)^2 dt. \quad (16)$$

The SNR from an eccentric MBHB, for a single pulsar, is thus given by the summation in quadrature over all the harmonics:

$$\left(\frac{S}{N}\right)^2 = \sum_{n=1}^\infty \frac{2}{S_k(f_n)} \int_{t_0}^t dt' s_n^2(t'), \quad (17)$$

while the total SNR in the PTA is given by the sum in quadrature of the SNRs produced in all the  $N_{\text{Pulsars}}$  included in the array:

$$\left(\frac{S}{N}\right)_{\text{tot}}^2 = \sum_{k=1}^{N_{\text{Pulsars}}} \left(\frac{S}{N}\right)_k^2. \quad (18)$$

Finally, the computation of the SNR of Eq. (17) requires a summation over all the harmonics, i.e  $n \in [1, +\infty]$ . However the contribution to the SNR goes to zero for  $n \rightarrow +\infty$  and the sum can be appropriately truncated. To select the harmonic of truncation,  $n_{\text{max}}$ , we adopted the simple criteria of  $n_{\text{max}} = 4n_{\text{peak}}$ , being  $n_{\text{peak}}$  the harmonic number at which the power of the GW emission is maximized for the selected eccentricity. To compute this value we follow the numerical fit presented in Hamers (2021):

$$n_{\text{peak}}(e) \simeq 2 \left( 1 + \sum_{k=1}^4 c_k e^k \right) (1 - e^2)^{-3/2}, \quad (19)$$

where  $c_1 = -1.01678$ ,  $c_2 = 5.57372$ ,  $c_3 = -4.9271$ ,  $c_4 = 1.68506$ . We have checked how the exact value of  $n_{\text{max}}$  affects our results. Specifically, less than 1% relative difference is seen in the SNR when it is computed assuming  $n_{\text{max}} = 10^4$  instead of  $n_{\text{max}} = 4n_{\text{peak}}$ .

#### 3.2. Parameter Estimation

Once the methodology to derive the SNR from an eccentric MBHB has been framed, the natural subsequent step is determining how well the system parameters can be measured. In the case of high SNR, they can be quickly estimated through the *Fisher Information Matrix* formalism. Specifically, the GW signal we are considering is characterized by 9 free parameters (see their definition in Section 2.1):

$$\lambda = (\zeta, f_k, e, i, \psi, l_0, \gamma, \phi, \theta). \quad (20)$$

To reconstruct the most probable source parameters,  $\lambda$ , given a set of data,  $\mathbf{d}$ , it is possible to work within the Bayesian framework and derive the posterior probability density function  $p(\lambda|\mathbf{d})$ :

$$p(\mathbf{d}|\lambda) \propto p(\lambda)p(\mathbf{d}|\lambda), \quad (21)$$

where  $p(\lambda|\mathbf{d})$  is the likelihood function and  $p(\lambda)$  is the prior probability density of  $\lambda$ . If we assume that near the maximum likelihood estimated value,  $\hat{\lambda}_i$ , the prior probability density is flat, the posterior distribution  $p(\lambda|\mathbf{d})$  will be proportional to the likelihood and can be approximated as a multi-variate Gaussian distribution:

$$p(\lambda|\mathbf{d}) \propto \exp \left[ -\frac{1}{2} \Gamma_{ij} \Delta\lambda_i \Delta\lambda_j \right], \quad (22)$$

where the indexes  $i$  and  $j$  run over all the components of the source parameter vector  $\lambda$  (in our case from 1 to 9), and  $\Delta\lambda_i = \hat{\lambda}_i - \lambda_i$  ( $\Delta\lambda_j = \hat{\lambda}_j - \lambda_j$ ) are the differences between the 'true' source parameters ( $\lambda$ ) and their most probable estimated values ( $\hat{\lambda}$ ). Finally,  $\Gamma_{ij}$  is the Fisher information matrix, and its

inverse provides a lower limit to the error covariance of unbiased estimators<sup>2</sup>. In the PTA case, the Fisher matrix is computed as:

$$\Gamma_{ij} = 4 \int_0^\infty df \frac{\partial_i s(f) \partial_j s(f)}{S_k(f)}, \quad (23)$$

where  $\partial_i$  and  $\partial_j$  are the partial derivatives of time residual in the frequency domain,  $s(f)$ , with respect to the  $\lambda_i$  and  $\lambda_j$  parameters, respectively. As for the SNR integral, the scalar product is defined in the frequency domain. However, we can apply the approximate identity given by Eq. (16) to write:

$$\Gamma_{ij} \approx \sum_{n=1}^{n_{\max}} \frac{2}{S_k(f_n)} \int_{t_0}^t dt' \partial_i s_n(t') \partial_j s_n(t'), \quad (24)$$

in which the partial derivatives are calculated numerically through:

$$\partial_i s_n(t) = \left[ \frac{s_n(t, \lambda_i + \delta\lambda_i/2) - s_n(t, \lambda_i - \delta\lambda_i/2)}{\delta\lambda_i} \right], \quad (25)$$

where the time step is set to be equal to  $\delta\lambda_i = 10^{-5}\lambda_i$ . We note that when calculating the SNR and the Fisher information matrix we always assume to know all the parameters that fully specify the residuals  $s(t)$ .

By assuming independent data streams for each pulsar in the array, the Fisher information matrix obtained from the full PTA,  $(\Gamma_{ij})_T$ , is simply given by the sum of the single Fisher information matrices derived for each pulsar,  $(\Gamma_{ij})_k$ :

$$(\Gamma_{ij})_{\text{tot}} = \sum_{k=1}^{N_{\text{pulsars}}} (\Gamma_{ij})_k. \quad (26)$$

We stress that the covariance matrix is simply the inverse of the Fisher information matrix ( $\Gamma^{-1}$ ), thus the elements on the diagonal represent the variances of the parameters ( $\sigma_{ii}^2 = \Gamma_{ii}^{-1}$ ), while the off-diagonal terms correspond to the correlation coefficients between parameters ( $\sigma_{ij}^2 = \Gamma_{ij}^{-1} / \sqrt{\sigma_i^2 \sigma_j^2}$ ).

### 3.3. Characterising the noise

The next fundamental ingredient in our computation is the noise description in PTA experiments. In particular, the pulsar NSPD can be broken down in two separate terms:

$$S_k(f) = S_h(f) + S_p(f). \quad (27)$$

The term  $S_h(f)$  describes the red noise contributed at each given frequency by the sGWB generated by the incoherent superposition of all the CGWs emitted by the cosmic population of adiabatically MBHBs (Rosado et al. 2015):

$$S_h(f) = \frac{h_c^2(f)}{12\pi^2 f^3}, \quad (28)$$

For a real PTA, the noise is estimated at each resolution frequency bin of the array. In fact if we assume an observation time  $T$ , the PTA is sensitive to an array of frequency bins  $\Delta f_i = [i/T, (i+1)/T]$ , with  $i = 1, \dots, N$ . If we now identify each

frequency bin  $\Delta f_i$  with its central frequency  $f_i$ , then we can associate to each frequency resolution element the characteristic strain produced by all the MBHBs emitting in that element as:

$$h_c^2(f_i) = \sum_{j=1}^{N_S} h_{c,j}^2(f) \delta(\Delta f_i - f). \quad (29)$$

where the sum is over all sources,  $N_S$ , and  $\delta(\Delta f_i - f)$  is a generalized delta function that assumes the value 1 when  $f \in \Delta f_i$ , and 0 otherwise, thus selecting only MBHBs emitting within the considered bin.  $h_{c,j}^2(f)$  is the squared characteristic strain of the  $j$ -th source. Since we consider eccentric MBHBs,  $h_{c,j}^2(f)$  is the sum of the strain emitted at all the harmonics  $nf_k$ , among which one has to select only those that lie within the frequency bin  $\Delta f_i$ . Eq. (29) thus generalizes to

$$h_c^2(f_i) = \sum_{j=1}^{N_S} \sum_{n=1}^{n_{\max}} h_{c,n,j}^2(nf_k) \delta(\Delta f_i - nf_k). \quad (30)$$

For each of the  $N_S$  binaries the value of  $h_{c,n}^2$  is given by:

$$h_{c,n}^2 = \frac{(\mathcal{A}^2 + \mathcal{B}^2)}{2} \frac{(GM_c)^{10/3}}{c^8 D_L^2} (2\pi f_k/n)^{4/3} \frac{g(n,e)}{(n/2)^2} \frac{nf_k}{\Delta f}, \quad (31)$$

where  $\mathcal{A} = 1 + \cos(i)$ ,  $\mathcal{B} = -2 \cos(i)$  and  $\Delta f = 1/T$  is the frequency bin width. The value of  $g(n, e)$  is computed according to:

$$g(n, e) = \frac{n^4}{32} \left( B_n^2 + (1 - e^2) A_n^2 + \frac{4}{3n^2} J_n(ne)^2 \right), \quad (32)$$

where  $A_n$  and  $B_n$  are:

$$\begin{aligned} B_n &= J_{n-2}(ne) - 2eJ_{n-1}(ne) + \frac{2}{n}J_n(ne) + 2eJ_{n+1}(ne) - J_{n+2}(ne), \\ A_n &= J_{n-2}(ne) - 2J_n(ne) + J_{n+2}(ne). \end{aligned} \quad (33)$$

We stress that when evaluating the detectability of a given MBHB we will not take into account the contribution of its  $h_{c,j}^2(f)$  when computing value of  $S_h(f)$ .

The term  $S_p(f)$  in the NSPD encodes all sources of noise unrelated to the sGWB, which are related to the telescope sensitivity, intrinsic noise in the pulsar emission mechanism, pulse propagation effects and so on. PTA collaborations parameterize the pulsar noise as a combination of three different terms:

$$S_p(f) = S_w + S_{\text{DM}}(f) + S_{\text{red}}(f). \quad (34)$$

$S_w$  accounts for processes that generate a white stochastic error in the measurement of a pulsar arrival time. These include pulse jitter, changes in the pulse profile with time, or instrumental artefacts. Such processes are uncorrelated in time and the resulting noise is modelled as  $S_w = 2\Delta t_{\text{cad}} \sigma_w^2$ , where it is commonly assumed that the pulse irregularity is a random Gaussian process described by the root mean square value  $\sigma_w$ .  $\Delta t_{\text{cad}}$  is the time elapsed between two consecutive observations of the same pulsar, i.e. the observation cadence.  $S_{\text{red}}(f)$  and  $S_{\text{DM}}(f)$  describe the achromatic and chromatic red noise contributions, respectively. While the former is the result of the pulsar intrinsic noise, the latter is the result of spatial variations in the interstellar electron content along the line of sight between the observer and the pulsar. These two red noises are usually modeled as a stationary stochastic process, described as a power law and fully characterized by an amplitude and a spectral index.

<sup>2</sup> For further details about the Fisher Information Matrix, we refer the reader to Husa (2009) and Sesana & Vecchio (2010).

## 4. Supermassive black hole binary populations and Pulsar Timing Arrays

### 4.1. The population of binaries

In this section, we briefly present the procedure used to generate the different populations of eccentric MBHBs that will be used throughout this paper. For further details, we refer the reader to [Sesana \(2010a, 2013b\)](#) and [EPTA Collaboration et al. \(2024\)](#).

To study the detectability of single MBHBs it is required to characterise their cosmological population as a whole. The sGWB spectrum generated by such a population can be calculated as the integrated emission of all the CGW signals emitted by individual binaries. Thus, the inclination and polarization average<sup>3</sup> characteristic strain of the sGWB can be expressed as:

$$h_c^2(f) = \int_0^\infty dz \int_0^\infty dm_1 \int_0^1 dq \frac{d^5 N}{dz dm_1 dq de d \ln f_{k,r}} \times \frac{32}{5} \frac{(GM_\tau)^{10/3}}{c^8 D_L^2 (1+z)^{4/3}} (2\pi f_{k,r})^{4/3} \sum_{n=1}^\infty \frac{g(n, e)}{(n/2)^2} \Big|_{f_{k,r}=f(1+z)/n}, \quad (35)$$

where  $d^5 N / (dm_1 dq dz de dt_r)$  is the comoving number of binaries emitting in a given logarithmic frequency interval,  $d \ln f_{k,r}$ , and primary mass, mass ratio, eccentricity and redshift in the range  $[m_1, m_1 + \delta m_1]$ ,  $[q, q + \delta q]$ ,  $[e, e + \delta e]$  and  $[z, z + \delta z]$ , respectively. In particular, this quantity can be re-written as:

$$\begin{aligned} \frac{d^5 N}{dz dm_1 dq de d \ln f_{k,r}} &= \frac{d^3 n}{dz dm_1 dq} \left( \frac{1}{f_{k,r}} \frac{df_{k,r}}{dt_r} \right)^{-1} \left[ \frac{dz}{dt_r} \frac{dV}{dz} \right] \\ &= \frac{d^3 n}{dz dm_1 dq} \left( \frac{1}{f_{k,r}} \frac{df_{k,r}}{dt_r} \right)^{-1} \frac{4\pi c D_L^2}{(1+z)}, \end{aligned} \quad (36)$$

where  $n = dN/dV$ ,  $d^3 n / (dz dm_1 dq)$  is the differential merger rate comoving density of MBHBs and  $f_{k,r} (dt_r / df_{k,r})$  represents the binary evolution timescale, which implicitly takes into account the variation of the hardening rate with the binary eccentricity (i.e. at fixed orbital frequency, eccentric binaries evolve faster). Following [Sesana \(2013b\)](#), the merger rate of MBHBs can be expressed in terms of the galaxy merger rate,  $(d^3 n_G / (dz dM_* dq_*))$ , as:

$$\begin{aligned} \frac{d^3 n}{dz dm_1 dq} &= \frac{d^3 n_G}{dz dM_* dq_*} \frac{dM_*}{dm_1} \frac{dq_*}{dq} = \\ &= \left[ \frac{\phi(M_*, z)}{M_* \ln 10} \frac{\mathcal{F}(z, M_*, q_*)}{\tau(z, M_*, q_*)} \frac{dt}{dz} \right] \frac{dM_*}{dm_1} \frac{dq_*}{dq}, \end{aligned} \quad (37)$$

where  $\phi(M_*, z)$  is the galaxy stellar mass function and  $\mathcal{F}(z, M_*, q_*)$  the differential fraction of galaxies with mass  $M_*$  at a given redshift paired with a satellite galaxy of mass in the interval  $[q_* M_*, (q_* + dq_*) M_*]$ <sup>4</sup>. The value  $\tau(z, M_*, q)$  is deduced from N-body simulations and corresponds to the typical merger timescale for a galaxy pair with a given mass, redshift and mass ratio. The term  $(dM_*/dm_1)(dq_*/dq)$  associates an MBH to each

<sup>3</sup> The sky and polarization average implies that  $(\mathcal{A}^2 + \mathcal{B}^2) = 64/5$

<sup>4</sup> Specifically,  $\mathcal{F}(z, M_*, q_*)$  was computed by setting  $\mathcal{F}(z, M_*, q_*) = -f_0(1+z)^\gamma / (q_* \ln q_m)$ , being  $f_0$  and  $\gamma$  free parameters inferred from observational studies and  $q_m$  the minimum mass ratio selected in counting pairs.

galaxy in the pair by using the MBH galaxy bulge mass scaling relation:

$$\log_{10}(M_{\text{BH}}) = \alpha + \beta \log_{10}(M_{\text{Bulge}}) + \mathcal{E} \quad (38)$$

where  $\mathcal{E}$  represents an intrinsic scatter, generally around 0.3–0.5 dex ([Sesana et al. 2016](#)), and  $\alpha$  and  $\beta$  define the zero point and logarithmic slope of the relation, respectively. To transform the total stellar mass into bulge mass, the relation  $M_* = f_b M_{\text{Bulge}}$  described in [Sesana et al. \(2016\)](#) is assumed.

Finally, the hardening of the binary in Eq. (36) is determined by using the stellar models of [Sesana \(2010b\)](#):

$$\begin{aligned} \frac{df_{k,r}}{dt_r} &= \left( \frac{df_{k,r}}{dt_r} \right)_* + \left( \frac{df_{k,r}}{dt_r} \right)_{\text{GW}} = \\ &= \frac{3G^{4/3}(m_1 + m_2)^{1/3} H \rho_i}{2(2\pi)^{2/3} \sigma_i} f_{k,r}^{1/3} + \frac{96(GM)^{5/3}}{5c^5} (2\pi)^{8/3} f_{k,r}^{11/3} \mathcal{F}(e), \end{aligned} \quad (39)$$

and

$$\begin{aligned} \frac{de}{dt_r} &= \left( \frac{de}{dt_r} \right)_* + \left( \frac{de}{dt_r} \right)_{\text{GW}} = \\ &= \frac{G^{4/3}(m_1 + m_2)^{1/3} \rho_i H K}{(2\pi)^{2/3} \sigma_i} f_{k,r}^{-2/3} - \frac{(GM)^{5/3}}{15c^5} (2\pi f_{k,r})^{8/3} \mathcal{G}(e), \end{aligned} \quad (40)$$

where

$$\begin{aligned} \mathcal{F}(e) &= \frac{1 + (73/24)e^2 + (37/96)e^4}{(1-e)^{7/2}}, \\ \mathcal{G}(e) &= \frac{304e + 121e^3}{(1-e^2)^{5/2}}, \end{aligned} \quad (41)$$

and  $\sigma_i$  and  $\rho_i$  are the velocity dispersion and stellar density at the binary influence radius.  $H$  and  $K$  represent the hardening rate and the eccentricity growth rate, calibrated against numerical three-body scattering experiments ([Sesana et al. 2006](#)).

#### 4.1.1. Generating MBHB populations consistent with PTA measurements

As described above, the cosmological coalescence rate of MBHBs depends on different assumptions about the galaxy merger rate and correlations between MBHBs and their hosts. In particular, the library of models presented in [Sesana \(2013b\)](#); [Rosado et al. \(2015\)](#); [Sesana et al. \(2016\)](#) combines a number of prescriptions from the literature which we summarize here:

1. *Galaxy stellar mass function.* Five different observational results are taken from the literature ([Borch et al. 2006](#); [Drory et al. 2009](#); [Ilbert et al. 2010](#); [Muzzin et al. 2013](#); [Tomczak et al. 2014](#)) and matched with the local mass function ([Bell et al. 2003](#)). For each of these functions, upper and lower limits were added to account for the errors given by the authors best-fit parameters. On top of this, an additional 0.1 dex systematic error was included to consider the uncertainties in the stellar masses determination. For all the mass functions, we separate between early/late-type galaxies and the analysis was restricted to  $z < 1.3$  and  $M_* > 10^{10} M_\odot$ , since we expect that these systems contribute the most to the sGWB signal (see e.g. [Sesana et al. 2009](#); [Kelley et al. 2018](#); [Izquierdo-Villalba et al. 2023](#))

2. *Differential fraction of paired galaxies.* The observational results of [Bundy et al. \(2009\)](#), [de Ravel et al. \(2009\)](#), [López-Sanjuan et al. \(2012\)](#) and [Xu et al. \(2012\)](#) were used when accounting for the evolution of the galaxy pair fraction.
3. *Merger timescale for a galaxy pairs.* We follow the fits done from the N-body and hydrodynamical simulations of [Kitzbichler & White \(2008\)](#) and [Lotz et al. \(2010\)](#).
4. *Galaxy-MBH scaling relation.* The masses assigned to each merging galaxy pair were drawn from several observational relations. However, given the high normalization of the observed PTA signal, we only considered relations presented by [Kormendy & Ho \(2013\)](#); [McConnell & Ma \(2013\)](#) and [Graham & Scott \(2013\)](#)

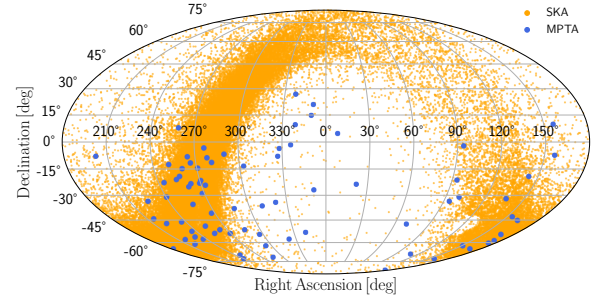


**Fig. 1.** Sky position of the pulsars included in the PTA experiments used in this work. The pulsars from MPTA are displayed in blue whereas the ones of SKA (full PsrPopPY population) are depicted in orange.

To save computation time, we perform an ad-hoc down-selection of the models, and limit our investigation to 108 combinations of the above prescriptions producing a distribution of sGWB amplitudes consistent with the measured PTA signal, as per Figure 2 of ([EPTA Collaboration et al. 2024](#)).

As for the environmental coupling and eccentricity evolution, we adopt the following prescriptions:

1. *Stellar density profile.* Following [Sesana \(2010b\)](#), the stellar density profile is assumed to be a broken power law following an isothermal sphere outside the influence radius,  $r_i = 1.2 \text{ pc } (M/10^6 M_\odot)^{0.5}$ , and a profile

$$\rho = C\rho_i \left(\frac{r}{r_i}\right)^{-1.5} \quad (42)$$

at  $r < r_i$ . Here,  $\rho_i = \sigma^2/(2\pi Gr_i^2)$  and  $\sigma$  is determined from the [Tremaine et al. \(2002\)](#) scaling relation (see [Sesana 2010b](#), for further details).  $C$  is a normalization factor of the stellar density profile and is assumed to take three different values (0.1, 1 and 10), to investigate the effect of changing the typical density of the environment.

2. *Initial eccentricity.* During the tracking of the hardening evolution, all the binaries are assumed to start with an initial eccentricity  $e_0$  at binary formation. Throughout the paper, we consider 10 initial values of  $e_0 = 0, 0.1, 0.2, 0.3, 0.4, 0.5, 0.6, 0.7, 0.8, 0.9$ .

Using the 108 population model, 10 eccentricity values and 3 environment normalizations defined above, we generate 3240 numerical distributions of MBHBs using Eq. (36), and for each distribution, we perform 10 Monte Carlo sampling for a gran total of 32400 MBHB populations. Each population consists of a list of  $\approx 10^5$  binaries characterized by their chirp mass, redshift, orbital frequency and eccentricity. Due to the computational cost required to compute the fisher information matrix, the latter has been calculated only for a subsample of 3240 populations (10% of the total).

#### 4.2. The array of pulsars

We explore the feasibility of detecting CGW signals using two different pulsar timing arrays: MeerKAT ( $N_{\text{Pulsars}} = 78$ ) and SKA ( $N_{\text{Pulsars}} = 200$ ). While pulsar monitoring at MeerKAT has been ongoing for 4.5 years, it will be superseded by the SKA

Mid array by 2027. Given these constraints, we choose 10 years for MeerKAT while the 30-year time span of SKA follows projections commonly used in the literature.

i) **MeerKAT** is a 64-antenna radio interferometer telescope located in South Africa. The regular monitoring of millisecond pulsar timing by MeerKAT is the basis of the MPTA. Recently, it was released the initial 2.5-years MPTA data ([Miles et al. 2023](#)). While the current data includes 88 pulsars, the release only contains the 78 pulsars that have at least 30 observations over this observing span, with a typical cadence of 14 days. The upper panel of Fig. 1 shows the position of those pulsars in the sky. Table A1 of [Miles et al. \(2023\)](#) also reported the noise properties of each of the 78 pulsars, accounting for white-noise terms, frequency-dependent DM variations, and an achromatic red-noise process (see Section 3.3). In this work, we will use a 10-year MPTA-like system, featuring the same set of pulsars (number, sky position, and noise model) as the one presented in [Miles et al. \(2023\)](#).

ii) **Square Kilometer Array Mid telescope (SKA, Dewdney et al. 2009)** planned to be operative in 2027, will be a large radio interferometer telescope whose sensitivity and survey speed will be an order of magnitude greater than any current radio telescope. For this work, we simulate a 30-year SKA PTA with 200 pulsars featuring a white noise of  $\sigma_w = 100 \text{ ns}$  and an observing cadence of 14 days. To picture a more realistic scenario we also include red noise to the total noise power spectral density in Eq. (34), parameterized as a power law (see e.g [Lentati et al. 2015](#)) of the form

$$S_{\text{red}}(f) = \frac{A_{\text{red}}^2}{12\pi^2} \left(\frac{f}{f_{\text{yr}}}\right)^{-\gamma_{\text{red}}} \text{ yr}^3, \quad (43)$$

where  $A_{\text{red}}$  the amplitude at one year and  $\gamma_{\text{red}}$  the spectral index. Red noise properties are drawn to be consistent with those measured in the EPTA DR2Full using the following procedure. We fit a linear  $\log A_{\text{red}} - \gamma$  relation to the measured red noises in Table 4 of [EPTA Collaboration et al. \(2023b\)](#). We then assign  $A_{\text{red}}$  and  $\gamma$  parameters consistent with this relation to 30% of the pulsars in the SKA array, drawing  $A_{\text{red}}$  randomly from a uniform log-distribution in the range to  $-15 < \log A_{\text{red}} < -14$ , for which the corresponding  $\gamma$  is  $> 3$ . In this way, we mimic in the SKA array the fraction and properties of EPTA DR2Full pulsars with a robust red noise contribution. Note that while the remaining 70% of the pulsars will likely display some lower level of red noise, this is unlikely to affect the properties of the detected CGWs. In

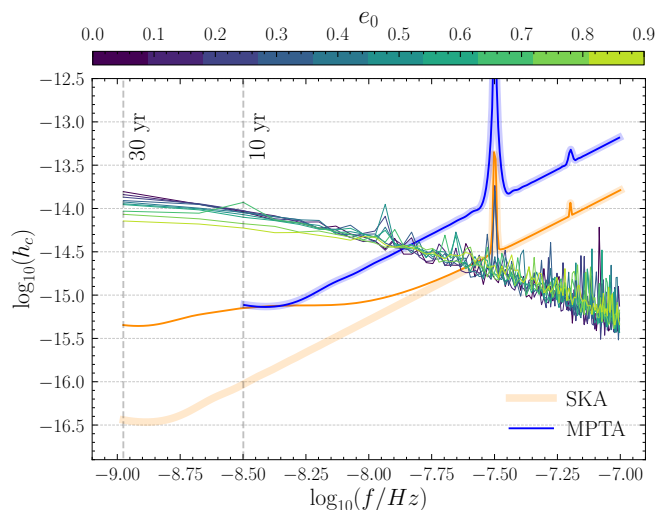


**Fig. 2.** Sensitivity curves of 10-year MPTA (blue) and 30-year SKA (orange) computed from HASASIA. The vertical dashed lines correspond to the frequency associated with the observing time span of MPTA and SKA (highlighted with vertical dashed lines). For completeness, the square mean of sGWB produced by our MBHB populations at different  $e_0$  models are represented in different colors. Pale (dark) blue and orange lines correspond to the MPTA and SKA sensitivity curves when accounting for pulsar white noise only (white plus red noise).

fact, for those pulsars the main stochastic red noise component is going to be the sGWB itself, which is already included in our calculation.

We then employ the pulsar population synthesis code `PsrPopPY`<sup>5</sup> (Bates et al. 2014) to draw a realistic distribution of pulsars in the array. `PsrPopPY` generates and evolves realistic pulsar populations drawn from physically motivated models of stellar evolution and calibrated against observational constraints on pulse periods, luminosities, and spatial distributions. The final population of pulsars ( $10^5$ ) is selected such that they would be observable ( $\text{SNR} > 9$ ) by a SKA survey with an antenna gain of 140 K/Jy and integration time of 35 minutes. In order to avoid a particularly lucky/unlucky pulsar sky disposition, from this distribution we select a different set of 200 pulsars for each one of the MBHB population presented in Section 4.1. The sky distribution of the whole pulsar sample of SKA is presented Fig. 1. Since `PsrPopPY` simulates hyper-realistic distributions of pulsars generated using theoretical considerations and observational constraints, the bulk of the generated full population of pulsars will lie close to the Galactic plane. However, the exceptional sensitivity of the SKA would also allow to choose the most isotropic distributions of pulsars in the PTA, maximizing sensitivity to any GW signals searched for by the PTA.

Fig. 2 presents the sensitivity curve of our SKA PTA and MPTA computed using HASASIA Python package (Hazboun et al. 2019). As expected, SKA PTA features better sensitivity than the MPTA. However, at low frequencies, both of them are limited by the sGWB. To guide the reader, Fig. 2 also displays the sensitivity curves of SKA and MeerKAT PTAs when only white noise is considered. As shown in Fig. 2, for MPTA the two sensitivity curves are almost identical since only 4 of the 78 pulsars listed in Miles et al. (2023) have a reported red noise.

<sup>5</sup> <https://github.com/samb8s/PsrPopPy>.

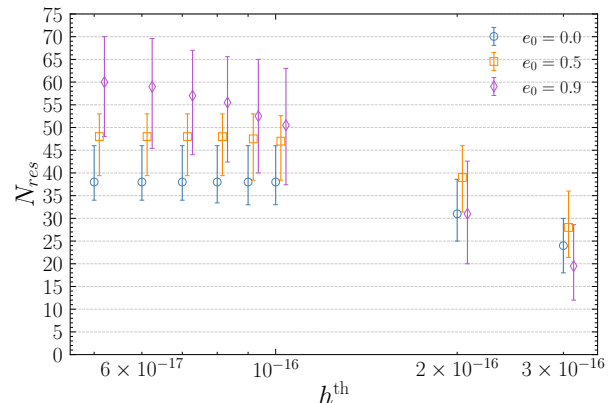


**Fig. 3.** Median number of resolvable sources of 96 randomly selected catalogs ( $N_{\text{res}}$ ), with three different initial eccentricity,  $e_0 = 0.0$ ,  $e_0 = 0.5$ ,  $e_0 = 0.9$ , as a function of the adopted thresholds in the GW signal amplitude ( $h^{\text{th}}$ ). Each set of marks and colors represents populations with different  $e_0$ , as labeled in the figure. The values of  $N_{\text{res}}$  are computed by using the SKA PTA.

Conversely, when achromatic red noise is included in the SKA PTA, due to the larger fraction of pulsars affected by it, the red noise slightly hider the array's sensitivity at the lowest frequencies ( $< 10^{-8}$  Hz).

#### 4.3. Identifying individually resolvable MBHB

To extract individually resolvable CGWs, we employ a recursive technique similar to Karnesis et al. (2021) and Pozzoli et al. (2023). We sort the MBHB population by strain amplitude according to the expression in Eq. (31), but selecting only the second harmonic ( $n = 2$ ). Following this ranking, we calculate the SNR of each source according to Eq. (18), including in the sGWB contribution to the noise the signals produced by all the other MBHBs. Whenever one source exceeds the  $\text{SNR} > 5$  for SKA or  $\text{SNR} > 3$  for MPTA, the source is deemed resolved and its contribution to the sGWB is subtracted. As a consequence, the level of the noise in the pulsar array is lowered as well (see Eq. (28)), making more feasible the detection of dimmer CGWs that might be otherwise unobservable. We therefore re-evaluate the detectability of all the remaining sources by making use of the new (lowered) background. This procedure is repeated until there are no resolvable sources left in the analyzed MBHB population.

The above recursive procedure must be applied to several thousands of MBHB populations, each including  $\sim 10^5$  systems, which becomes extremely time-consuming. To boost the efficiency of our pipeline, we established a criterion that allows us to select only those sources with the largest chance of being resolvable. We established a threshold in the value of  $h = 2\zeta G^{5/3}(\pi f_k)^{2/3}/c^4$  (hereafter  $h^{\text{th}}$ ) below which we do not compute the SNR, deeming the source too dim to be resolved. To determine the exact value of the threshold, we have computed the number of resolvable sources ( $N_{\text{res}}$ ) at different  $h^{\text{th}}$  cuts for 96 randomly selected MBHB catalogs at three different values of  $e_0$ . We imposed the condition  $\text{SNR} > 5$  for CGW detection and computed the number of resolvable sources using the SKA PTA, because of its larger performance in resolving dim GW sources compared to MPTA. Since, for this analysis, we are interested in the dimmest MBHB that the PTA experiment can resolve, we conservatively consider SKA PTA which features only white

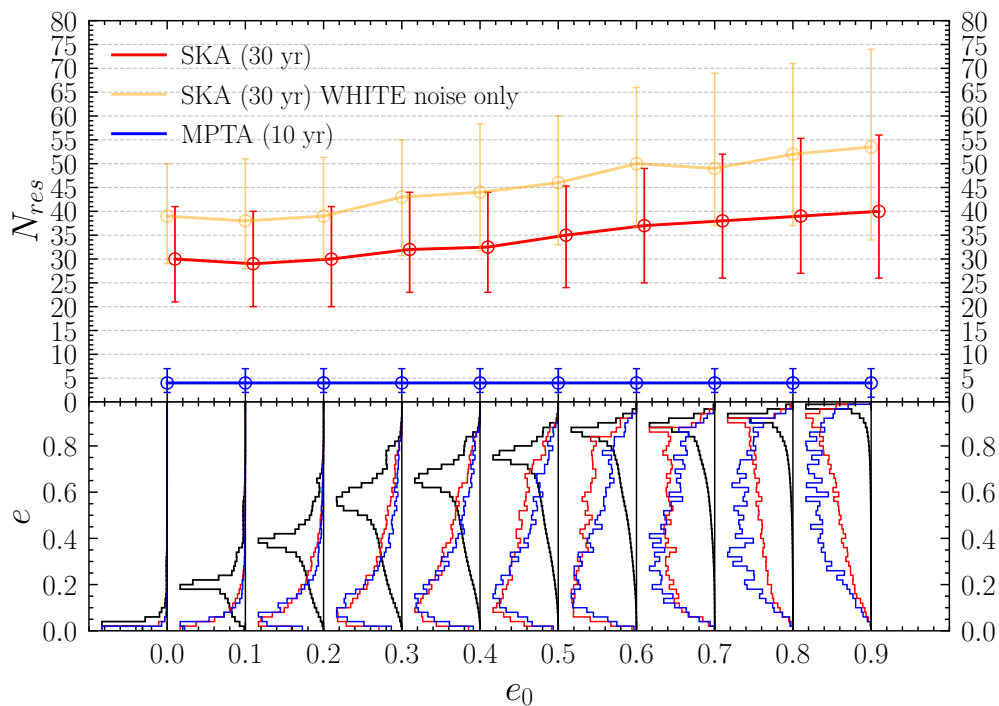


**Fig. 4.** Number of resolvable sources ( $N_{\text{res}}$ ) for as a function of  $e_0$ . Open dots represent median values from all the considered MBHB population models, while error bars represent the 84 and 16 percentile of the distribution. Blue points correspond to the results of 10-year MPTA data with  $\text{SNR} > 3$ , while the red ones represent the predictions for 30-year SKA data with  $\text{SNR} > 5$ . Orange points represent the 30-year SKA results but when accounting only for the white pulsar noise. The lower panel shows the eccentricity distribution of the whole MBHB population for different  $e_0$  models (black) and the eccentricity distribution of the MBHBs detectable as CGW sources ( $e_{\text{rs}}$ ) for SKA PTA (orange) and for MPTA (blue). Note that all the distributions are normalized to the same peak value for visualization purposes.

noise. Fig. 3 shows the median number of  $N_{\text{res}}$  as a function of  $h^{\text{th}}$ . As expected,  $N_{\text{res}}$  increases towards small values of  $h^{\text{th}}$ , but it saturates below a certain threshold. This behavior is seen for all  $e_0$  used to start the MBHB evolution. Taking into account Fig. 3, throughout this work we will use the conservative value of  $h^{\text{th}} = 6 \times 10^{-17}$ . We stress that small fluctuations are seen in the  $N_{\text{res}}$  median below our fiducial threshold. However, they are not statistically significant ( $\pm 1$  source) and the selected  $h^{\text{th}}$  provides a good compromise between accuracy and computational efficiency. The recursive SNR evaluation-subtraction procedure is thus performed only on the subset of binaries with  $h > h^{\text{th}}$ , providing a considerable speedup of the calculation.

## 5. Results

In this section, we present the main results of our work. The analysis has been performed taking into account different values of  $e_0$ . This has enabled us to characterize the effect of eccentricity in determining the number of resolvable sources and the accuracy of the parameter estimation from the detected signal. To avoid confusion with the initial eccentricity used in the hardening model,  $e_0$ , throughout the whole section we will tag the eccentricity of the detected MBHB as  $e_{\text{rs}}$ .

### 5.1. Number of resolvable sources

The upper panel of Fig. 4 shows the median number of resolvable sources ( $N_{\text{res}}$ ) detected by the SKA and MPTA. The results have been divided according to the eccentricity at which the MBHB population was initialized ( $e_0$ ). This classification

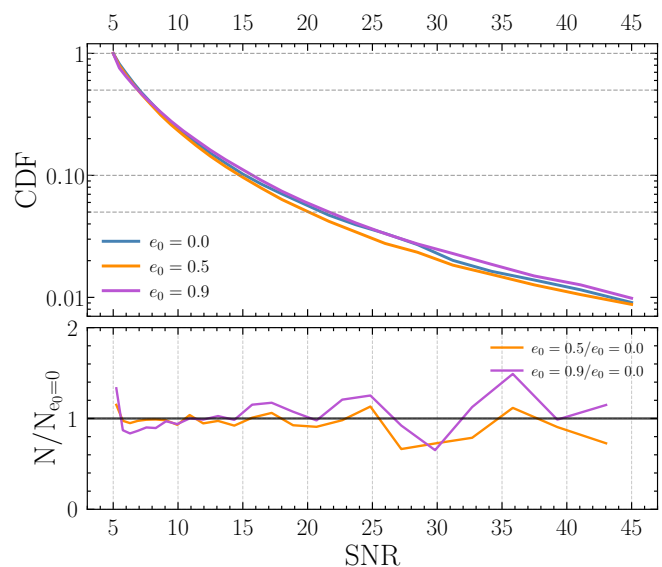


**Fig. 5.** Cumulative distribution function (CDF) of the SNR featured by MBHBs detected by 30-year SKA PTA. Blue, orange, and purple curves represent the CDF of all the models generated with  $e_0 = 0, 0.5$  and  $0.9$ , respectively. The lower panel presents the number of sources found with a given value of SNR for  $e_0 = 0.5$  and  $e_0 = 0.9$  models (orange and purple line) normalized with the same value found in the  $e_0 = 0$  case.

allows us to understand the role of the eccentricity of the global MBHB population on the prospects of CGW detection. The

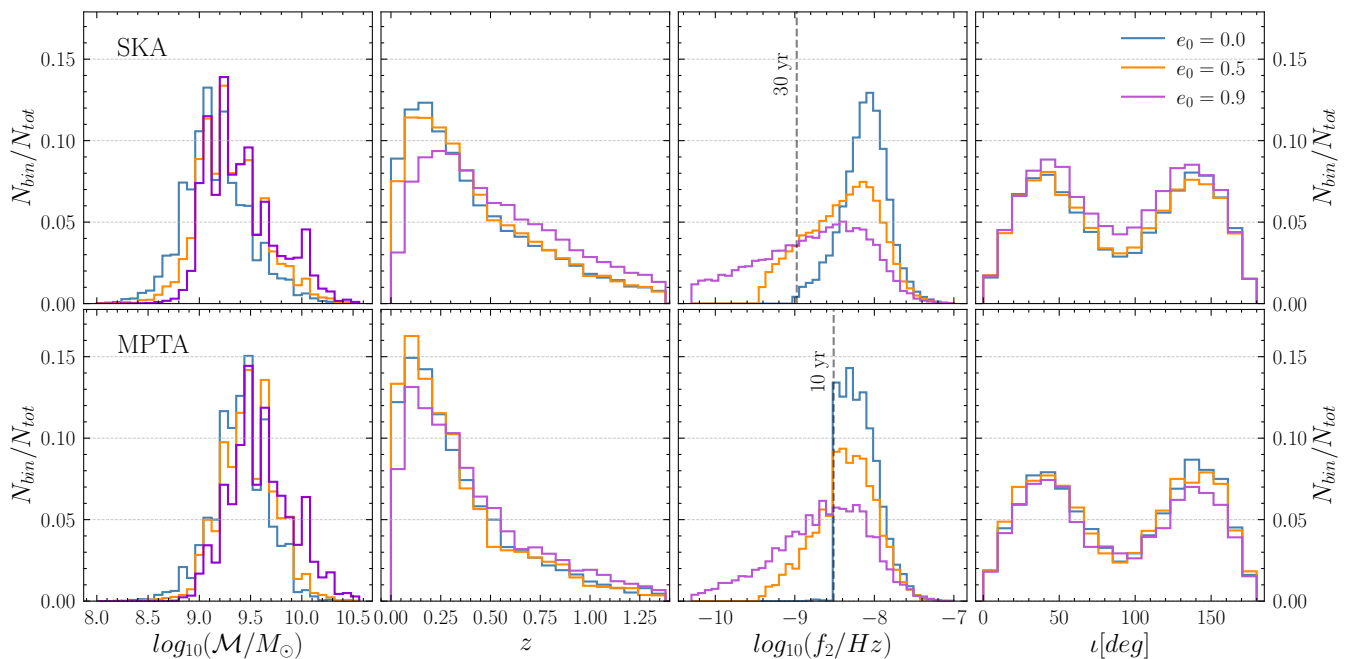


**Fig. 6.** Chirp mass distribution ( $\mathcal{M}$ , upper left panel), redshift ( $z$ , upper right panel), twice the observed Keplerian frequency ( $f_2$ , lower left panel), and inclination angle ( $i$ , lower right panel) of the detected MBHBs. Each color represents the distributions when different eccentricity values are used to evolve the MBHB population ( $e_0 = 0$ , blue,  $e_0 = 0.5$ , orange and  $e_0 = 0.9$  purple).  $N_{Bin}$  represents the number of objects in a given bin of the histogram while  $N_{tot}$  is the total number of objects analyzed. While the upper panels represent the results for 30-year SKA PTA, the lower ones correspond to 10-year MPTA.

median number of resolvable sources for 10-year MPTA is 4, independently of  $e_0$ . Conversely, 30-years SKA provides larger  $N_{res}$  values ( $\sim 35$ ), increasing with eccentricity. In particular, the number of detected binaries starts to increase when  $e_0 > 0.2$ . This trend can be ascribed to the appearance of resolvable high-eccentric MBHBs with observed Keplerian frequency outside of the PTA frequency range. Given their large eccentricity, these systems can push a large fraction of their GW signal inside the PTA band (more details in the description of Fig. 6 and Fig. 7 below). The eccentricity distribution of the detected MBHBs is presented in the lower panel of Fig. 4. Regardless of the adopted array, the eccentricity distribution of resolved sources peaks at lower values compared to the underlying overall MBHB population. Therefore, the eccentricity of the detected systems is not a good tracer of the eccentricity of the global MBHB population. This is because the more massive binaries, which circularize faster (see Eq. 40), are also the more likely to be detected. Compared to MPTA, SKA PTA can generally observe more eccentric MBHBs, which is expected due to its longer timespan. In fact, the SKA PTA sensitivity extends to lower frequencies, where MBHBs had less time to circularize due to GW emission. For completeness, Fig. 4 depicts the number of resolvable sources for SKA PTA when only the pulsar white noise is taken into account. As shown, when the red noise is neglected the number of resolvable sources increases by  $\sim 30\%$ .

Finally, Fig. 5 shows the distribution of the SNR of resolvable sources. For clarity, we only presented the results for the SKA PTA given that MPTA features the same trends (but extended down to SNR = 3). As we can see, 90% of the detected systems present SNR < 15, but there is a large tail towards larger values. Despite being just a few, the remaining 10% of sources with SNR > 15 will be optimal targets for multimessenger astronomy, since their sky localization will be small enough to

perform electromagnetic follow-ups (see Section 3.2 and Goldstein et al. 2019). Finally, to compare the SNR distributions for models initialized with different eccentricities we compute the ratio between the number of sources at different SNR bins for  $e_0 = 0.5, 0.9$  by the detected population with  $e_0 = 0.0$ . As can be seen, no major differences in the SNR distribution are found.

## 5.2. Properties of the resolvable sources

In this section, we study the properties of the resolvable sources and explore possible dependencies with the eccentricity of the underlying MBHB population. For the sake of clarity, the analysis has been done only using three reference eccentricity models:  $e_0 = 0.0, 0.5$  and  $0.9$ .

The left panels of Fig. 6 present the chirp mass distribution of the MBHB population detected by SKA and MPTA experiments. As shown, both PTAs will detect MBHBs with  $\mathcal{M} \sim 10^{9.5} M_\odot$ , although MPTA will be biased towards more massive systems given its lower sensitivity. Interestingly, the detection of  $\mathcal{M} \lesssim 10^9 M_\odot$  binaries by SKA is preferred when the underlying MBHB population is initialized with low eccentricities ( $e_0 < 0.5$ ). This is due to the typical eccentricity and observed Keplerian frequency of  $\mathcal{M} < 10^9 M_\odot$  systems. These MBHBs are placed at  $f_k \sim 10^{-8.5}$  Hz independently of  $e_0$ , but their eccentricity raises when  $e_0$  increases (e.g.  $\sim 0.4$  and  $\sim 0.6$  for  $e_0 = 0.5, 0.9$  models, respectively). These relatively high values of  $f_k$  and eccentricity cause these systems to emit part of their GW strain at high frequencies where the PTA sensitivity is already degrading. The net effect is the decrease of the source SNR with respect to a non-eccentric case. To illustrate this, the top panel of Fig. 7 presents the characteristic GW strain versus observed GW frequency for three binaries

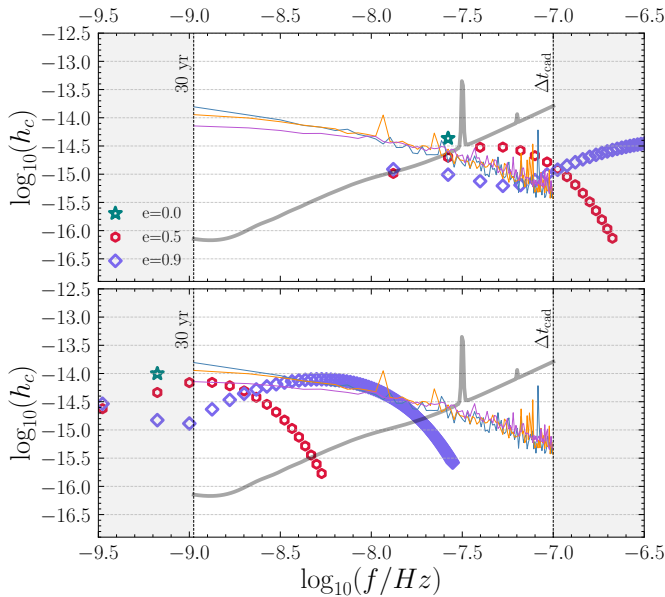


**Fig. 7.** Characteristic strain ( $h_c$ ) as a function of observed frequency ( $f$ ). The upper panel shows a binary with  $M \sim 10^{8.5} M_\odot$  and the observed Keplerian frequency  $f_k \sim 10^{-8}$  Hz; while the lower panel shows a binary of  $M \sim 10^{10} M_\odot$  and  $f_k \sim 10^{-9.5}$  Hz outside the SKA PTA sensitivity curve. In each panel, blue, orange, and purple lines represent the root mean square of the sGWB generated by all the models with  $e_0 = 0, 0.5$  and  $0.9$ , respectively. The black line corresponds to the sensitivity curve of SKA PTA (white and red noise) 30-year data. The colored dots represent how the signal of an MBHB is distributed across different frequencies when the eccentricity is varied between  $0, 0.5$  and  $0.9$ .

with the same mass and Keplerian frequency but different eccentricities. As shown, for circular binaries all the emitted power falls in the frequency region in which the PTA has the best sensitivity. However, for the extreme case of  $e > 0.5$  most of the power is pushed at  $f > 3 \times 10^{-8}$  Hz where the PTA is the less sensitive. Consequently, our analysis suggests that the detection of low-mass MBHBs ( $M < 10^9 M_\odot$ ) will be hindered in highly eccentric populations.

The redshift distribution of the resolvable sources is presented in the middle-left panels of Fig. 6. The distribution peaks at  $z < 0.25$ , independently of the PTA experiment used and the eccentricity of the underlying MBHB population. The SKA resolved population has a longer tail at high redshifts, due to its better sensitivity. Moreover, there is a small trend towards higher redshifts with increasing eccentricity, more prominent in SKA than MPTA. The frequency distribution of the resolved binaries is shown in the middle-right panels of Fig. 6. The peak of the distribution seats around  $\sim 10^{-8.5} - 10^{-8}$  Hz, being systematically higher for SKA PTA given its better sensitivity at high frequencies. As anticipated in Section 5.1, models with eccentric binaries enable the detection of MBHBs whose  $f_2 = 2f_k$  is smaller than the minimum frequency allowed by the PTA observing time. In the extreme case of  $e_0 = 0.9$ , up to half of the detected systems display this feature in the MPTA array. An illustrative example of how the strain is distributed among all the harmonics for a source with Keplerian frequency outside the PTA band can be seen in the lower panel of Fig. 7. Finally, the inclination distribution shown in the rightmost panels of Fig. 6 is bimodal, preferring face-on/face-off binaries with respect to the observer ( $i < 50$  deg and  $i > 125$  deg). This is simply due to the

angular pattern emission of GWs, which are stronger along the binary orbital angular momentum axis.

### 5.3. SMBHB parameter estimation

Here, we explore the precision to which the CGW source parameters can be determined. To this end, we make use of the procedure presented in Section 3.2. We focus on parameters of astrophysical relevance. Specifically, the GW amplitude,  $\zeta$ , the observed Keplerian frequency,  $f_k$ , the orbital eccentricity,  $e_{rs}$ , the inclination angle,  $i$ , and the initial orbital phase,  $l_0$ . The latter parameters might help the identification of distinctive electromagnetic counterparts. In fact, accreting binaries at low inclination angles might appear as Type I AGN, displaying considerable variability in the optical/UV, while relativistic jets could be observable for nearly face-on systems (e.g. Fedrigo et al. 2024; Gutiérrez et al. 2024). Moreover, precise phase determination of eccentric binaries allows to clearly identify the periastron passage epochs, which can be associated to a dimming in the electromagnetic emission due to temporary mini-disc disruptions caused by the close flyby of the two MBHBs (Cocchiararo et al. 2024). Finally, we combine the two angles defining the source position in the sky to determine the 2D sky localization uncertainty as (Sesana & Vecchio 2010):

$$\Delta\Omega = 2\pi \sqrt{(\sin\theta\Delta\theta\Delta\phi)^2 - (\sin\theta\sigma_{\theta\phi})^2}, \quad (44)$$

where  $\sigma_{\theta,\phi}$  is the correlation coefficient between  $\theta$  and  $\phi$  computed from the Fisher matrix. With this definition the probability of a GW source to be found outside a certain solid angle  $\Delta\Omega_0$  is proportional to  $e^{-\Delta\Omega_0/\Delta\Omega}$ . Consequently,  $\Delta\Omega$  is an important quantity to take into account given that it provides information about the accuracy of pinpointing the GW source in the sky. Moreover, its specific value will shed light on the possibility of carrying out multimessenger studies by placing constraints on the size of the area to scan for electromagnetic follow-ups (see, e.g., Lops et al. 2023; Petrov et al. 2024).

Results are presented in Fig. 8 for the SKA PTA as a function of the eccentricity of the detected source,  $e_{rs}$ , to determine its potential impact on the parameter estimation. MPTA parameter estimation features the same trends and is shown in Appendix A. Since the estimation precision depends on the source SNR, we have performed this exploration at fixed bins of SNR:  $3 < \text{SNR} < 10$ ,  $10 < \text{SNR} < 15$ , and  $\text{SNR} > 15$ . For each case, we show the median value on the error of the parameter recovery and the central 68% of the distribution. The recovery of the GW amplitude displays a small correlation with  $e_{rs}$ , slightly improving for high eccentric binaries. For instance, the median relative error for systems with  $\text{SNR} > 15$  and  $e_{rs} < 0.1$  is  $\sim 30\%$  while for high eccentric cases is reduced down to  $\sim 20\%$ . As it is the case for all parameters, the GW amplitude recovery precision scales linearly with the inverse of the SNR. Notably, while at  $\text{SNR} > 15$  the source amplitude can be determined with a median relative error of 0.2-0.3, at  $\text{SNR} < 10$  it is poorly constrained. Conversely, the Keplerian frequency is extremely well determined, with a relative error that is always smaller than 1%. In this case, the trend with eccentricity is reversed, with the median error increasing with  $e_{rs}$ . The error associated with the binary eccentricity improves for highly eccentric systems, with values as low as  $\sim 1 - 5\%$  at  $e_{rs} > 0.6$ . The inclination of the MBHB orbit is essentially unconstrained, especially for systems at small SNR and for small eccentricities. The initial phase of the orbit displays a

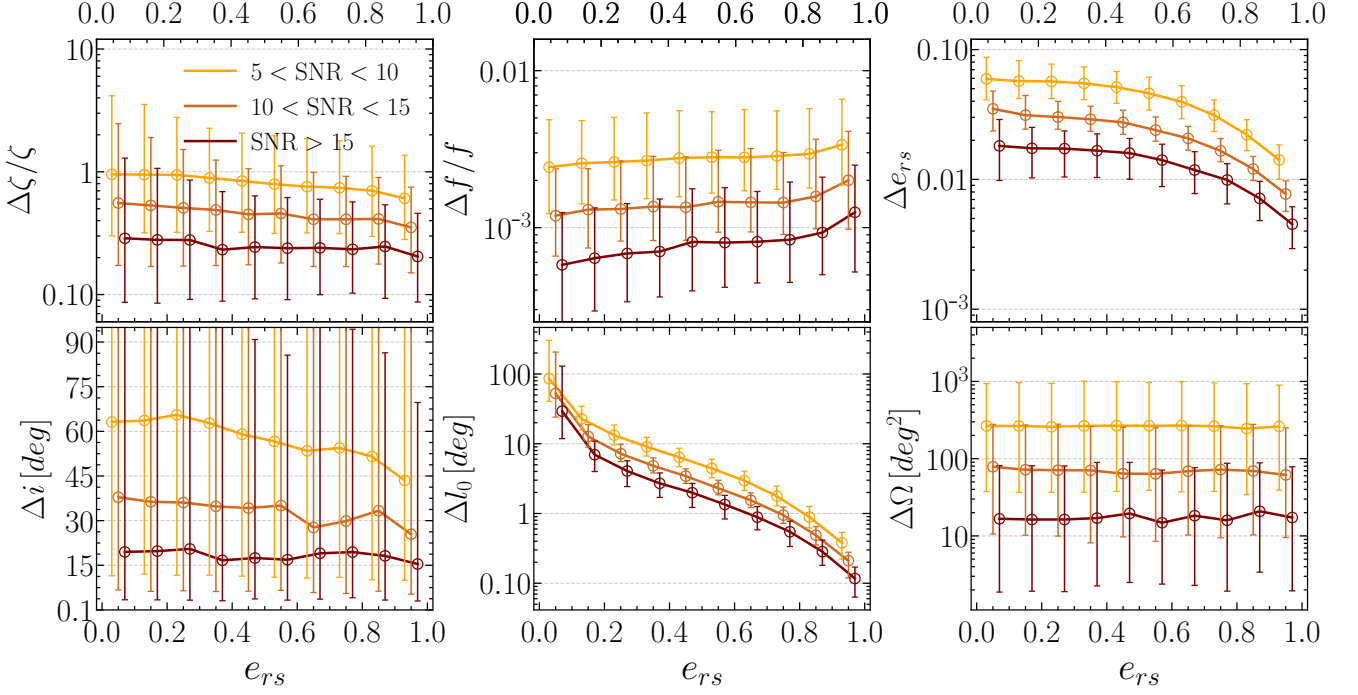


**Fig. 8.** Accuracy in recovering the source parameters as a function of the eccentricity of the detected source,  $e_{rs}$ : GW amplitude ( $\Delta\zeta/\zeta$ , top left), Keplerian frequency ( $\Delta f/f$ , top middle), eccentricity ( $\Delta e_{rs}$ , top right), inclination angle ( $\Delta i$ , bottom left), the initial phase of the orbit ( $\Delta l_0$ , bottom middle) and sky localization ( $\Delta\Omega$ , bottom right). All the results have been divided into three different SNR bins  $3 < \text{SNR} < 10$  (orange),  $10 < \text{SNR} < 15$  (dark orange) and  $\text{SNR} > 15$  (dark red).

clear dependence on  $e_{rs}$ , being better constrained for large eccentric cases. For instance, at  $10 < \text{SNR} < 15$   $\Delta l_0$  associated with  $e_{rs} < 0.2$  MBHB is  $\sim 10$  deg while it drops down to  $\sim 1$  deg for  $e_{rs} > 0.6$ . This is not surprising since for an eccentric orbit GW emission is strongly localized close to the pericenter, allowing a precise measurement of the orbital phase of the system.

Finally, the lower right panel of Fig. 8 presents the sky-localization. Interestingly, it does not show any dependence with  $e_{rs}$  but, as expected, it strongly improves with SNR, since the parameter has a theoretical scaling with  $\text{SNR}^{-2}$ . Binaries detected at  $5 < \text{SNR} < 10$  have a median sky-localization of  $\Delta\Omega \sim 200$  deg<sup>2</sup>, making multimessenger follow-ups extremely challenging. On the other hand, systems with  $\text{SNR} > 15$  feature median  $\Delta\Omega \sim 20$  deg<sup>2</sup>. Note that the 68% confidence region extends down to  $\approx 2$  deg<sup>2</sup>. Since SKA can resolve 30-40 binaries and about 10% of them will have  $\text{SNR} > 15$  (see Fig. 5), we can therefore expect at least one CGW with source localization at the  $\sim$ deg<sup>2</sup> level, which would be a perfect target for electromagnetic follow-ups.

## 6. Caveats

In this section, we discuss the main caveats and assumptions related to the methodology.

### 6.1. Time evolving binaries

We have assumed that the MBHB orbital frequency does not evolve during the PTA observation time. However, this simplification may not hold, especially for massive and high-frequency binaries given their shorter GW timescales (see Eq. 39). To explore the fraction of MBHBs in our catalogues in which the non-evolving assumption is not fulfilled, we have computed the fol-

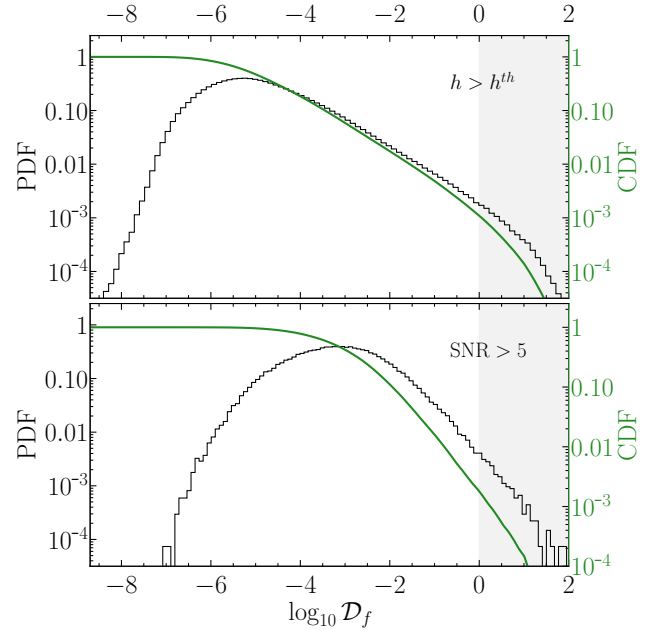


**Fig. 9.** Probability distribution function (PDF) of  $\mathcal{D}_f$  for binaries featuring  $h > h^{\text{th}}$  (top panel) and binaries detected by SKA PTA ( $\text{SNR} > 5$ , bottom panel). In both panels, green lines correspond to the cumulative distribution function (CDF).

lowing quantity:

$$\mathcal{D}_f = \frac{\left[ \frac{df_s}{dt} T_{\text{obs}} \right]}{\Delta f}. \quad (45)$$

Here  $df_k/dt$  is determined according to Eq. (39) but for simplicity accounting only the GW term, while the factor  $(df_k/dt) \times T_{obs}$  corresponds to the variation of the observed Keplerian frequency over the PTA observational time. The division by  $\Delta f$  accounts for the total variation of the MBHB frequency within the frequency bin width given by the PTA observation span. The upper panel of Fig. 9 presents the distribution of  $\mathcal{D}_f$  for all the binaries in our catalogue whose  $h > h^{th}$  (see Section 4.3). As shown, the distribution peaks at low values of  $\mathcal{D}_f$  ( $\sim 10^{-6}$ ), implying an almost null evolution of the binary frequency. Nevertheless, some cases show  $\mathcal{D}_f > 1$ , but they correspond to less than 0.1% of the MBHB population. The lower panel of Fig. 9 presents the  $\mathcal{D}_f$  distribution only for the subset of sources that are resolvable by SKA PTA. Not surprisingly, the distribution for this sub-sample of binaries peaks at larger values. This shift is caused by the fact that individually resolvable MBHBs are intrinsically systems with large masses and high frequencies (see Fig. 6). Despite this, the bulk of the system feature  $\mathcal{D}_f \sim 10^{-3}$ , consistent again with non-evolving binaries. Also for this sub-sample, binaries with  $\mathcal{D}_f > 1$  only account for 0.1% of the resolvable sources. In light of these results, we can conclude that our assumption of non-evolving binaries can be safely adopted.

### 6.2. Pericenter precession

Another assumption that is relevant to discuss concerns the inclusion of the pericenter precession. To quantify its impact on the SNR recovery, we adopted the same criteria presented in Sesana & Vecchio (2010). The precession of the pericenter induces an additional shift in the observed Keplerian frequency given by  $f_k + \dot{\gamma}/\pi$  with

$$\dot{\gamma} = \frac{d\gamma}{dt} = 6\pi f_k \frac{(2\pi f_k(1+z)MG)^{2/3}}{(1-e^2)c^2}. \quad (46)$$

This causes a bias in the recovery of the orbital frequency. However, this effect can be neglected as long as the shift caused by pericenter precession over the observed time is small compared to the frequency resolution of the detector,  $\Delta f$ . This is equivalent to enforce the condition  $\mathcal{D}_\gamma \ll 1$ , where:

$$\mathcal{D}_\gamma = \frac{\left[ \frac{d^2\gamma}{dt^2} T_{obs} \right]}{\Delta f}, \quad (47)$$

with:

$$\frac{d^2\gamma}{dt^2} = \frac{96(2\pi)^{13/3}}{(1-e^2)c^7} [(1+z)M]^{2/3} \mathcal{M}_\zeta^{5/3} G^{7/3} f_k^{13/3}. \quad (48)$$

Fig. 10 shows the distribution of  $\mathcal{D}_\gamma$  for all MBHBs with  $h > h^{th}$  (top panel) and for those detected by the SKA PTA (lower panel). Similar to the  $\mathcal{D}_f$  result, the systems with  $\mathcal{D}_\gamma > 1$  represent only 0.1% of the resolved MBHBs. As a consequence, the effect of the pericenter precession can be ignored for our astrophysical-motivated populations of MBHBs.

### 6.3. Pulsar term

Similarly to other works, we did not account for the pulsar term since its inclusion in the matched filtering methodology requires a precise estimate of the distance between the pulsar and the Earth. Up to date, only a very reduced sample of pulsars has such

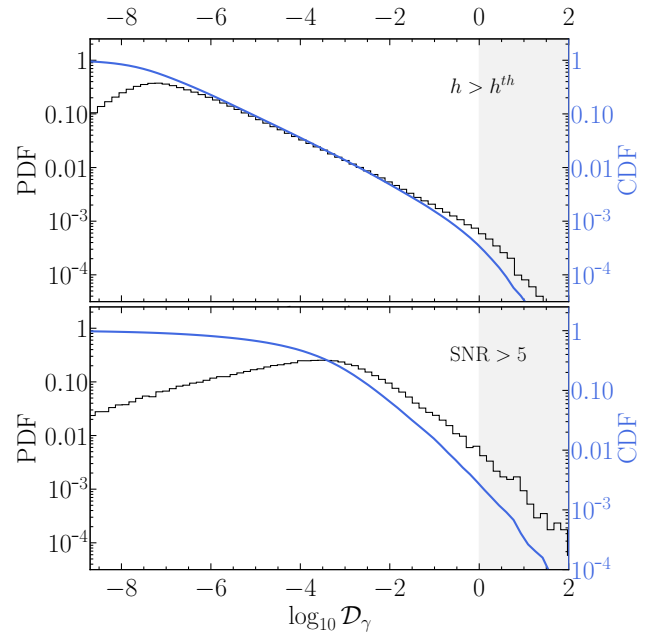


**Fig. 10.** Probability distribution function (PDF) of  $\mathcal{D}_\gamma$  for binaries featuring  $h > h^{th}$  (top panel) and binaries detected by SKA PTA ( $\text{SNR} > 5$ , bottom panel). In both panels, blue lines correspond to the cumulative distribution function (CDF).

an accurate measurement of this quantity. Despite this, ongoing efforts are being made to calculate the pulsar distance via the measurement of pulsar spin down and annual parallax motion (see e.g. Reardon et al. 2016).

When it comes to 2D sky localization, including the Pulsar term in the analysis does not appear to make a significant difference in the size of the localization area, at least in the case of circular, GW-driven binaries. It can, however, cause a small bias compared to the true sky location (Ferranti et al. in prep.). Therefore, while Earth term-only estimates are robust in terms of localization precision, including the pulsar term in the analysis might be required to pinpoint the correct direction in the sky.

Including the pulsar term in the CGW searches could also provide key information on how the MBHB evolves during the times needed for the pulse to cover the Earth-Pulsar distance. Under the assumption of GW-driven binaries, identification of the pulsar term allows to effectively separate the system chirp mass from the distance in the signal amplitude parameter  $\zeta$  (Ferranti et al. in prep for examples involving circular binaries), greatly improving 3D localization of the source in the sky. This assumption, however, is not necessarily fulfilled. At the low frequencies probed by PTAs, MBHBs can be still coupled to their environment, especially at the time of Pulsar-term production. In fact, since the typical Earth-Pulsar separation can range up to thousands of light years, the Pulsar and Earth terms of the signal could inform us about the binary properties at two different evolutionary stages. In this case, the change of parameters such as the orbital frequency and the eccentricity could help to better understand the environment in which the MBHB resided. As shown in Eq. (39), the Keplerian frequency of a binary evolving only due to GW emission varies as  $\propto f^{11/3}$ , while if its dynamics is ruled by stellar scattering events, it changes as  $\propto f^{1/3}$ . Including environmental coupling, however, increases the number of parameters in the model, and whether GW and environmental

effects can be efficiently separated in a real analysis has still to be investigated.

#### 6.4. Further complications in source detectability

Throughout this work, we used a simple SNR criterion to define source detectability, regardless of the nature of the GW signal. However, the shape of the waveform can be significantly different for circular and highly eccentric binaries and while the detectability of the former has been extensively demonstrated in the literature (Babak & Sesana 2012; Ellis et al. 2012; Ellis 2013), much less has been done on the eccentric binary front (Taylor et al. 2016). This is especially true for sources with  $f_2 < 1/T$ , which can constitute up to 50% of the resolvable CGWs in the limit of high eccentricities for the MPTA (see Fig. 6). For these systems, the waveform consists of a single burst-like spike coincident with the binary periastron passage (e.g. Amaro-Seoane et al. 2010), which is very different from a repeated sinusoidal pattern. Although analytical templates can certainly be constructed for such signals, the effectiveness of match filtering in extracting them from real data has still to be investigated.

## 7. Conclusions

In this work, we studied the capability of future PTA experiments of detecting single MBHBs under the natural assumption that the sGWB is produced by an eccentric MBHB population. To this end, we have generalized the standard approach used in PTA to assess the observability of circular MBHBs, by computing the SNR and Fisher Information Matrix for eccentric systems. We have adopted a 10-year MPTA and 30-year SKA PTAs and applied our analysis to a wide number of simulated eccentric MBHB populations, compatible with the latest measured amplitude of the sGWB. The main results can be summarized as follows:

- The expected number of resolvable sources detected by a 10-year MPTA ( $\text{SNR} > 3$ ) is  $4_{-2}^{+3}$  (68% credible interval) with no dependence on the eccentricity of the underlying MBHB population.
- The extraordinary sensitivity of a 30-year SKA PTA will enable the detection of  $30_{-10}^{+11}$  (68% credible interval) sources with  $\text{SNR} > 5$  for initially circular MBHB population. This number grows to  $40_{-15}^{+15}$  in the case of very high MBHB initial eccentricity ( $e_0 = 0.9$ ). This is mostly caused by highly eccentric binaries with Keplerian frequency  $\lesssim 10^9$  Hz pushing part of their power into the SKA sensitivity band.
- The resolved MBHBs do not follow the eccentricity distribution of the underlying MBHB population. Instead, they tend to favor lower eccentricities. This is caused by the fact that the bulk of the detected MBHB population is placed in the frequency range  $10^{-8.5} - 10^{-8}$  Hz. At those frequencies, GW emission is expected to dominate and, as a consequence, partial circularization of the binary orbit has already taken place. Practically, this means that massive and high-frequency systems, most likely to be detected, should display low eccentricities with respect to the bulk of the population.
- The chirp mass ( $\mathcal{M}$ ) of the resolvable sources is  $\gtrsim 10^{8.5} M_\odot$ , but it depends on the specific PTA experiment. While the

median value for MPTA is  $\sim 10^{9.5} M_\odot$ , that for SKA shifts down to  $\sim 10^9 M_\odot$ . The results also show that the detection of binaries with  $\mathcal{M} \lesssim 10^9 M_\odot$  is strongly disfavored, especially when the eccentricity of the underlying MBHB population is large.

- The distribution of resolvable sources peaks at  $z < 0.25$ , regardless of the PTA used but, unsurprisingly, it is more skewed towards low- $z$  for MPTA. Their typical frequency at the second harmonic ( $f_2$ ) sits at  $\sim 10^{-8.5}$  Hz for SKA PTA and increases to  $\sim 10^{-8}$  Hz for MPTA. The eccentricity of the MBHB population shifts the  $f_2$  median value towards low frequencies. This is caused by the fact that highly eccentric populations have a significant number of resolvable sources with  $f_2 < 1/T_{\text{obs}}$ . Finally, the inclination between the MBHB and the observer shows a bi-modal distribution with maximum probability for face-one configurations. No correlation with the eccentricity of the MBHB population is seen.
- The accuracy of recovering the source properties shows a mild dependence on the eccentricity of the system. Whereas the frequency, amplitude, and orbital inclination are almost independent of it, the eccentricity and initial orbital phase of the MBHB orbit show a clear trend. Specifically (and unsurprisingly), these parameters are better constrained for sources with large eccentricities.
- The sky-localization does not show any dependence on the MBHB eccentricity. However, it roughly follows the expected  $\text{SNR}^{-2}$  trend. In particular, binaries detected with  $5 < \text{SNR} < 10$  feature a median  $\Delta\Omega \sim 200 \text{ deg}^2$ , hindering any possible multimessenger follow-up. MBHBs with  $\text{SNR} > 15$  display a median  $\Delta\Omega \sim 20 \text{ deg}^2$ . We note that the scatter around these median values is up to 1dex (68% confidence), due to the anisotropy of the pulsar distribution and intrinsic properties of the MBHB population. In the most optimistic case, we can expect 30-yr SKA to localize a particularly loud MBHB at a  $\sim \text{deg}^2$  accuracy.

In this work, we developed a theoretical framework to assess the detectability and parameter extraction of eccentric MBHB from realistic populations. This allowed us to investigate the performance of future radio facilities such as MPTA and SKA. Being able to fully detect the presence of single MBHB sources at nHz frequencies will be fundamental in determining the astrophysical or cosmological nature of the signal recently reported by worldwide PTAs and will open the era of multimessenger astronomy with MBHBs. In a future work, we plan to implement the procedure presented here in the populations of galaxies, MBHs and MBHBs generated by galaxy formation models to explore the capabilities of associating CGW sources detected by PTAs with galaxies and AGNs.

*Acknowledgements.* We thank the B-Massive group at Milano-Bicocca University for useful discussions and comments. R.T., D.I.V., A.S. and G.M.S acknowledge the financial support provided under the European Union's H2020 ERC Consolidator Grant "Binary Massive Black Hole Astrophysics" (B Massive, Grant Agreement: 818691). M.B. acknowledges support provided by MUR under grant "PNRR - Missione 4 Istruzione e Ricerca - Componente 2 Dalla Ricerca all'Impresa - Investimento 1.2 Finanziamento di progetti presentati da giovani ricercatori ID:SOE\_0163" and by University of Milano-Bicocca under grant "2022-NAZ-0482/B".

## References

- Afzal, A., Agazie, G., Anumarlapudi, A., et al. 2023, *ApJ*, 951, L11
- Agazie, G., Anumarlapudi, A., Archibald, A. M., et al. 2023a, *ApJ*, 951, L8
- Agazie, G., Anumarlapudi, A., Archibald, A. M., et al. 2023b, *ApJ*, 951, L8
- Amaro-Seoane, P., Sesana, A., Hoffman, L., et al. 2010, *MNRAS*, 402, 2308
- Anholm, M., Ballmer, S., Creighton, J. D. E., Price, L. R., & Siemens, X. 2009, *Phys. Rev. D*, 79, 084030
- Antoniadis, J., Arumugam, P., Arumugam, S., et al. 2023, arXiv e-prints, arXiv:2306.16226
- Arzoumanian, Z., Brazier, A., Burke-Spolaor, S., et al. 2015, *ApJ*, 810, 150
- Babak, S. & Sesana, A. 2012, *Phys. Rev. D*, 85, 044034
- Barack, L. & Cutler, C. 2004, *Phys. Rev. D*, 69, 082005
- Bates, S. D., Lorimer, D. R., Rane, A., & Swiggum, J. 2014, *MNRAS*, 439, 2893
- Begelman, M. C., Blandford, R. D., & Rees, M. J. 1980, *Nature*, 287, 307
- Bell, E. F., McIntosh, D. H., Katz, N., & Weinberg, M. D. 2003, *ApJS*, 149, 289
- Bonetti, M., Rasskazov, A., Sesana, A., et al. 2020, *MNRAS*, 493, L114
- Book, L. G. & Flanagan, É. É. 2011, *Phys. Rev. D*, 83, 024024
- Borch, A., Meisenheimer, K., Bell, E. F., et al. 2006, *A&A*, 453, 869
- Bortolas, E., Bonetti, M., Dotti, M., et al. 2022, *MNRAS*, 512, 3365
- Bortolas, E., Capelo, P. R., Zana, T., et al. 2020, *MNRAS*, 498, 3601
- Bundy, K., Fukugita, M., Ellis, R. S., et al. 2009, *ApJ*, 697, 1369
- Burke-Spolaor, S. 2013, *Classical and Quantum Gravity*, 30, 224013
- Cocchiararo, F., Franchini, A., Lupi, A., & Sesana, A. 2024, arXiv e-prints, arXiv:2402.05175
- Cuadra, J., Armitage, P. J., Alexander, R. D., & Begelman, M. C. 2009, *MNRAS*, 393, 1423
- de Ravel, L., Le Fèvre, O., Tresse, L., et al. 2009, *A&A*, 498, 379
- Desvignes, G., Caballero, R. N., Lentati, L., et al. 2016, *MNRAS*, 458, 3341
- Detweiler, S. 1979, *ApJ*, 234, 1100
- Dewdney, P. E., Hall, P. J., Schilizzi, R. T., & Lazio, T. J. L. W. 2009, *IEEE Proceedings*, 97, 1482
- Dotti, M., Colpi, M., Haardt, F., & Mayer, L. 2007, *MNRAS*, 379, 956
- Dressler, A. & Richstone, D. O. 1988, *ApJ*, 324, 701
- Drory, N., Bundy, K., Leauthaud, A., et al. 2009, *ApJ*, 707, 1595
- Ellis, J. A. 2013, *Classical and Quantum Gravity*, 30, 224004
- Ellis, J. A., Jenet, F. A., & McLaughlin, M. A. 2012, *ApJ*, 753, 96
- EPTA Collaboration, InPTA Collaboration, Antoniadis, J., et al. 2023a, *A&A*, 678, A50
- EPTA Collaboration, InPTA Collaboration, Antoniadis, J., et al. 2024, *A&A*, 685, A94
- EPTA Collaboration, InPTA Collaboration, Antoniadis, J., et al. 2023b, *A&A*, 678, A49
- Escala, A., Larson, R. B., Coppi, P. S., & Mardones, D. 2004, *ApJ*, 607, 765
- Faber, S. M. 1999, *Advances in Space Research*, 23, 925
- Fastidio, F., Gualandris, A., Sesana, A., Bortolas, E., & Dehnen, W. 2024, arXiv e-prints, arXiv:2406.02710
- Fedrigo, G., Cattorini, F., Giacomazzo, B., & Colpi, M. 2024, *Phys. Rev. D*, 109, 103024
- Fiacconi, D., Mayer, L., Roškar, R., & Colpi, M. 2013, *ApJ*, 777, L14
- Foster, R. S. & Backer, D. C. 1990, *ApJ*, 361, 300
- Franchini, A., Lupi, A., & Sesana, A. 2022, *ApJ*, 929, L13
- Franchini, A., Sesana, A., & Dotti, M. 2021, *MNRAS*, 507, 1458
- Gardiner, E. C., Kelley, L. Z., Lemke, A.-M., & Mitridate, A. 2023, arXiv e-prints, arXiv:2309.07227
- Genzel, R., Hollenbach, D., & Townes, C. H. 1994, *Reports on Progress in Physics*, 57, 417
- Genzel, R. & Townes, C. H. 1987, *ARA&A*, 25, 377
- Goldstein, J. M., Sesana, A., Holgado, A. M., & Veitch, J. 2019, *MNRAS*, 485, 248
- Graham, A. W. & Scott, N. 2013, *ApJ*, 764, 151
- Gualandris, A., Khan, F. M., Bortolas, E., et al. 2022, *MNRAS*, 511, 4753
- Gutiérrez, E. M., Combi, L., Romero, G. E., & Campanelli, M. 2024, *MNRAS*, 532, 506
- Haehnelt, M. G. & Rees, M. J. 1993, *Monthly Notices of the Royal Astronomical Society*, 263, 168
- Hamers, A. S. 2021, *Research Notes of the American Astronomical Society*, 5, 275
- Häring, N. & Rix, H.-W. 2004, *ApJ*, 604, L89
- Hazboun, J., Romano, J., & Smith, T. 2019, *The Journal of Open Source Software*, 4, 1775
- Hellings, R. W. & Downs, G. S. 1983, *ApJ*, 265, L39
- Hopkins, P. F., Richards, G. T., & Hernquist, L. 2007, *ApJ*, 654, 731
- Husa, S. 2009, *General Relativity and Gravitation*, 41, 1667
- Ilbert, O., Salvato, M., Le Floch, E., et al. 2010, *ApJ*, 709, 644
- Izquierdo-Villalba, D., Sesana, A., & Colpi, M. 2023, *MNRAS*, 519, 2083
- Jaffe, A. H. & Backer, D. C. 2003, *ApJ*, 583, 616
- Karnesis, N., Babak, S., Pieroni, M., Cornish, N., & Littenberg, T. 2021, *Phys. Rev. D*, 104, 043019
- Kelley, L. Z., Blecha, L., Hernquist, L., Sesana, A., & Taylor, S. R. 2018, *MNRAS*, 477, 964
- Kitzbichler, M. G. & White, S. D. M. 2008, *MNRAS*, 391, 1489
- Kocsis, B. & Sesana, A. 2011, *MNRAS*, 411, 1467
- Kormendy, J. 1988, *ApJ*, 325, 128
- Kormendy, J. & Ho, L. C. 2013, *ARA&A*, 51, 511
- Kormendy, J. & Richstone, D. 1992, *ApJ*, 393, 559
- Kramer, M. & Champion, D. J. 2013, *Classical and Quantum Gravity*, 30, 224009
- Lacey, C. & Cole, S. 1993, *MNRAS*, 262, 627
- Lee, K. J. 2016, in *Astronomical Society of the Pacific Conference Series*, Vol. 502, *Frontiers in Radio Astronomy and FAST Early Sciences Symposium 2015*, ed. L. Qain & D. Li, 19
- Lentati, L., Taylor, S. R., Mingarelli, C. M. F., et al. 2015, *MNRAS*, 453, 2576
- Li, K., Bogdanović, T., Ballantyne, D. R., & Bonetti, M. 2022, *ApJ*, 933, 104
- López-Sanjuan, C., Le Fèvre, O., Ilbert, O., et al. 2012, *A&A*, 548, A7
- Lops, G., Izquierdo-Villalba, D., Colpi, M., et al. 2023, *MNRAS*, 519, 5962
- Lotz, J. M., Jonsson, P., Cox, T. J., & Primack, J. R. 2010, *MNRAS*, 404, 575
- Manchester, R. N., Hobbs, G., Bailes, M., et al. 2013, *PASA*, 30, e017
- Mayer, L., Kazantzidis, S., Madau, P., et al. 2007, *Science*, 316, 1874
- McConnell, N. J. & Ma, C.-P. 2013, *ApJ*, 764, 184
- McLaughlin, M. A. 2013, *Classical and Quantum Gravity*, 30, 224008
- Merloni, A. & Heinz, S. 2008, *MNRAS*, 388, 1011
- Miles, M. T., Shannon, R. M., Bailes, M., et al. 2023, *MNRAS*, 519, 3976
- Muzzin, A., Marchesini, D., Stefanon, M., et al. 2013, *ApJ*, 777, 18
- O'Dowd, M., Urry, C. M., & Scarpa, R. 2002, *ApJ*, 580, 96
- Peterson, B. M., Ferrarese, L., Gilbert, K. M., et al. 2004, *ApJ*, 613, 682
- Petrov, P., Taylor, S. R., Charisi, M., & Ma, C.-P. 2024, arXiv e-prints, arXiv:2406.04409
- Phinney, E. S. 2001, arXiv e-prints, astro
- Planck Collaboration, Ade, P. A. R., Aghanim, N., et al. 2014, *A&A*, 571, A16
- Pozzoli, F., Babak, S., Sesana, A., Bonetti, M., & Karnesis, N. 2023, *Phys. Rev. D*, 108, 103039
- Quinlan, G. D. & Hernquist, L. 1997, *New A*, 2, 533
- Ravi, V., Wyithe, J. S. B., Shannon, R. M., Hobbs, G., & Manchester, R. N. 2014, *MNRAS*, 442, 56
- Reardon, D. J., Hobbs, G., Coles, W., et al. 2016, *MNRAS*, 455, 1751
- Reardon, D. J., Zic, A., Shannon, R. M., et al. 2023, *ApJ*, 951, L6
- Rosado, P. A., Sesana, A., & Gair, J. 2015, *MNRAS*, 451, 2417
- Savorgnan, G. A. D., Graham, A. W., Marconi, A. r., & Sani, E. 2016, *ApJ*, 817, 21
- Sazhin, M. V. 1978, *Soviet Ast.*, 22, 36
- Schmidt, M. 1963, *Nature*, 197, 1040
- Sesana, A. 2010a, *ApJ*, 719, 851
- Sesana, A. 2010b, *ApJ*, 719, 851
- Sesana, A. 2013a, *Classical and Quantum Gravity*, 30, 224014
- Sesana, A. 2013b, *MNRAS*, 433, L1
- Sesana, A., Haardt, F., & Madau, P. 2006, *ApJ*, 651, 392
- Sesana, A. & Khan, F. M. 2015, *MNRAS*, 454, L66
- Sesana, A., Shankar, F., Bernardi, M., & Sheth, R. K. 2016, *MNRAS*, 463, L6
- Sesana, A. & Vecchio, A. 2010, *Phys. Rev. D*, 81, 104008
- Sesana, A., Vecchio, A., & Volonteri, M. 2009, *MNRAS*, 394, 2255
- Susobhanan, A., Maan, Y., Joshi, B. C., et al. 2021, *PASA*, 38, e017
- Taylor, S. R. 2021, arXiv e-prints, arXiv:2105.13270
- Taylor, S. R., Huerta, E. A., Gair, J. R., & McWilliams, S. T. 2016, *ApJ*, 817, 70
- Tomczak, A. R., Quadri, R. F., Tran, K.-V. H., et al. 2014, *ApJ*, 783, 85
- Tremaine, S., Gebhardt, K., Bender, R., et al. 2002, *ApJ*, 574, 740
- Ueda, Y., Akiyama, M., Hasinger, G., Miyaji, T., & Watson, M. G. 2014, *ApJ*, 786, 104
- Vasiliev, E., Antonini, F., & Merritt, D. 2014, *ApJ*, 785, 163
- Vestergaard, M. & Peterson, B. M. 2006, *ApJ*, 641, 689
- White, S. D. M. & Frenk, C. S. 1991, *ApJ*, 379, 52
- White, S. D. M. & Rees, M. J. 1978, *MNRAS*, 183, 341
- Xu, C. K., Shupe, D. L., Béthermin, M., et al. 2012, *ApJ*, 760, 72
- Xu, H., Chen, S., Guo, Y., et al. 2023, *Research in Astronomy and Astrophysics*, 23, 075024
- Yu, Q. 2002, *MNRAS*, 331, 935

## Appendix A: Accuracy in the recovery of SMBHB parameters for the MPTA case

In this section, we investigate the accuracy of recovering the binary parameters when using the 10-year MPTA. We point out that at very high eccentricities the results are noisy given that in MPTA these types of binaries are rarer than in SKA PTA (see lower panel of Fig 4). For these reasons, the results above  $e_{\text{rs}} > 0.8$  are affected by low statistics and should be taken with caution.

Fig. A.1 presents the results. As shown, the errors in the parameter estimation for the 10-year MPTA generally follow the same trend as the ones for SKA. This confirms that the main driving factor in parameter estimation is the signal-to-noise ratio. Notably, the error in the frequency is worse in MPTA than in SKA at a fixed SNR. This is because the frequency resolution of the PTA is set by the observation time  $T_{\text{obs}}$ . The second interesting result regards the better estimation of the source sky location for MPTA with respect to SKA. This is because the sky position of the MPTA pulsars follows a more isotropic distribution. Hence, is able to better triangulate the GW source sky position. On the contrary for SKA PTA we select an ultra-realistic pulsar sky distribution, and hence most of the pulsars are located inside the Galactic plane. This highlights the need to choose a distribution of pulsars in the sky as isotropic as possible.

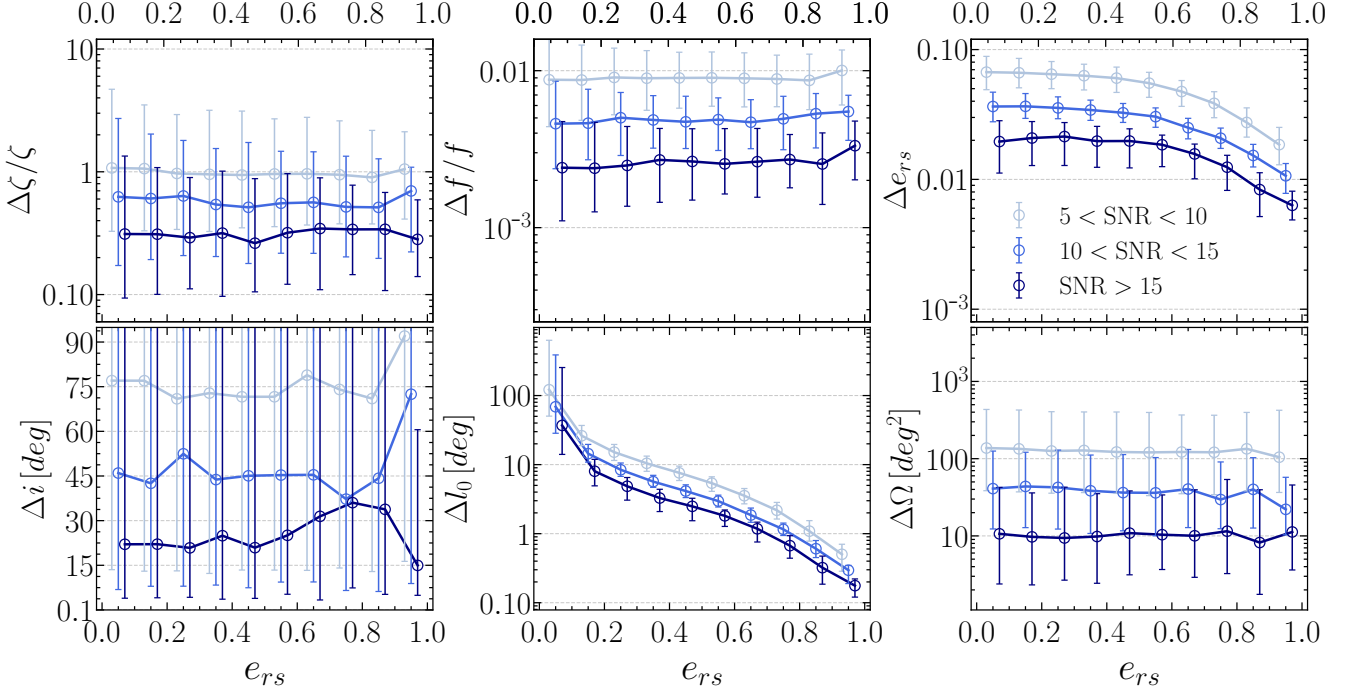


**Fig. A.1.** Accuracy for 10-yr MPTA in recovering the source parameters as a function of the eccentricity of the detected source,  $e_{rs}$ : GW amplitude ( $\Delta\zeta/\zeta$ , top left), Keplerian frequency ( $\Delta f/f$ , top middle), eccentricity ( $\Delta e_{rs}$ , top right), inclination angle ( $\Delta i$ , bottom left), the initial phase of the orbit ( $\Delta l_0$ , bottom middle) and sky localization ( $\Delta\Omega$ , bottom right). All the results have been divided into three different SNR bins  $3 < \text{SNR} < 10$  (pale blue),  $10 < \text{SNR} < 15$  (blue) and  $\text{SNR} > 15$  (dark blue).